Supplement of Atmos. Chem. Phys., 18, 17769–17800, 2018
https://doi.org/10.5194/acp-18-17769-2018-supplement

Supplement of

Secondary organic aerosol production from local emissions dominates the organic aerosol budget over Seoul, South Korea, during KORUS-AQ

Benjamin A. Nault et al.

Correspondence to: Jose L. Jimenez (jose.jimenez@colorado.edu)

S1. KORUS-AQ Overview

Table S1. List of NASA DC-8 research flights and date of take-off. Unless noted, the take-off dates are different than the local dates since the data was recorded in UTC. We document the research flights with the UTC dates to correspond with the data repository (Aknan and Chen, 2018).

Research Flight Number	*Date of Take-off*	*Regions Sampled*	*Number of Seoul Missed Approaches*
01	01/May/2016	Jeju jetway (×2)	3
02	03/May/2016	Yellow Sea, Jeju jetway	3
03	04/May/2016	Jeju jetway	2
04	06/May/2016	Busan jetway (×2)	3
05	10/May/2016	Jeju jetway, other[b]	2
06	11/May/2016	Yellow Sea, other[c]	3
07	12/May/2016	Yellow Sea, other[d]	0
08	16/May/2016	Jeju jetway, Busan jetway	3
09	17/May/2016	Yellow Sea, Busan jetway	3
10	19/May/2016	Busan jetway (×2)	3
11	21/May/2016	Yellow Sea	3
12	24/May/2016	Yellow Sea	2
13	26/May/2016[a]	Jeju Jetway	2
14	29/May/2016	Yellow Sea, Busan jetway	4
15	30/May/2016	Yellow Sea, Jeju jetway	3
16	01/June/2016	Busan jetway, Jeju jetway	3
17	02/June/2016	Busan jetway, Jeju jetway	3
18	04/June/2016	Yellow Sea, other[e]	5
19	08/June/2016	Busan jetway (×2)	3
20	09/June/2016	Jeju jetway, other[b]	2

[a] For RF13, the DC-8 took-off after 00:00 UTC, corresponding to the date in local time and UTC time being the same.

[b] The DC-8 sampled south of the Korean peninsula.

[c] The DC-8 sampled east of Seoul to the Sea of Japan.

[d] The DC-8 sampled the Sea of Japan.

[e] The DC-8 remained in the greater Seoul area to sample point sources.

Table S2. Description of the geographical locations used in Figure 1 and throughout the text, and shown in Figure S1..

Location	*Lat Min (°N)*	*Lat Max (°N)*	*Lon Min (°E)*	*Lon Max (°E)*
Seoul	36.8	37.6	124.6[a]	128.0
Yellow Sea			124.0	126.0
Jeju jetway	34.2	36.8	126	127
Busan jetway	35.2	36.8	128.6	129.9

[a] This value was chosen to include the Seoul outflow observed during RF11 and RF18.

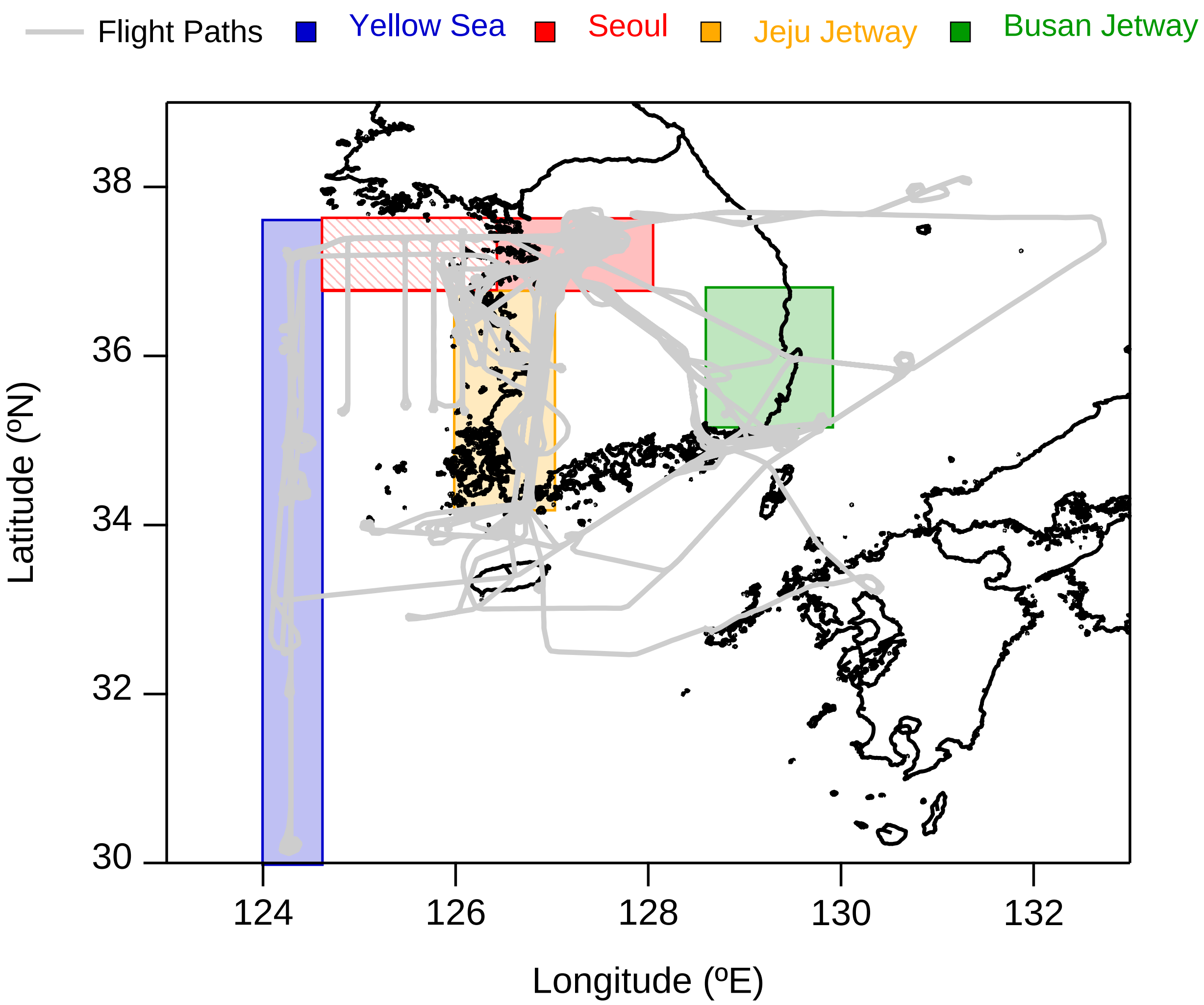

Figure S1. Geographical regions shown in SI Table 1. Note, the Seoul box is extended into the Yellow Sea to capture the outflow of Seoul emissions for two flights (RF11 and RF18).

S2. CU-AMS Sampling and Calibration

After almost every flight, the ionization efficiency (IE) was calibrated (Figure S3) using the single particle technique. Briefly, air containing 150 – 250 particles/cm^3 of NH_4NO_3, of 400 nm (mobility diameter, sized with a differential mobility analyzer, TSI model 3080, that was installed in the same rack as the CU-AMS) was sampled by the AMS. Thresholds of 4 (*m/z* 30) or 3 (*m/z* 46) ions per event were selected to produce a low, but detectable background (typically ~7 events/cm^3 background). An event would be recorded, after evaporation and ionization of NH_4NO_3 particle, if at least 4 (*m/z* 30) or 3 (*m/z* 46) ions were observed. These values were analyzed using the ToF AMS Ionization Efficiency Calibration Panel for ET, v1.0.5F (http://cires1.colorado.edu/jimenez-group/ToFAMSResources/ToFSoftware/index.html#ToF_IE_Cal), to process the data and calculate IE and IE/AB (AB is air beam). Typical values during KORUS-AQ, for 400 nm (mobility diameter) NH_4NO_3 calibrations were the following: 10 baseline segments and minimum and maximum ions per particle values of 1 and 200. During KORUS-AQ, the average IE/AB was $8.10(\pm 0.64)\times 10^{-13}$ ions/molecule of nitrate, which leads to an overall 10% variability for this value during the whole campaign. Further details about using single particle technique for IE/AB calibrations can be found in Nault et al. (2016).

These IE calibrations also provided relative ionization efficiency (RIE) calibrations of NH_4 after nearly every flight, as well (Figure S3), along with the NO^+ and NO_2^+ ratios of ammonium nitrate, which are useful to estimate particle organic nitrate concentrations, as detailed in Fry et al. (2013). The SO_4 and Chl RIEs were measured about once every week, and the interpolated values were used for the SO_4 and Chl concentrations. For the organic aerosol, we used an RIE of 1.4 (Jimenez et al., 2016; Xu et al., 2018). Finally, to test the effects of solution mixtures on RIE for

SO_4 and NH_4, we made calibration solutions ranging from 0 – 100% NH_4NO_3, with the balance coming from $(NH_4)_2SO_4$. We find no effects, both on the calculated NH_4 balance (Figure S6), when using the NH_4 and SO_4 RIE's from the pure calibration, and on the recalculated NH_4 (SO_4) RIE when keeping a constant SO_4 (NH_4) RIE from the pure calibrations (Figure S6). The consistency in the NH_4 balance, as observed in prior studies (Docherty et al., 2011; Jimenez et al., 2016), and the high precision (3% precision in all calculations) provides further confidence in the stability of the RIEs for the species in calculating their mass in mixed particles, and indicates that there are no effects on the RIE with changing composition, and, thus, CE (Jimenez et al., 2016).

Also, the IE calibrations performed after each flight provided an opportunity to calculate the effect of pNO_3 on producing a small artifact CO_2^+ signal, as detailed in Pieber et al. (2016), and of pNO_3 on producing small artifact HCl^+ and Cl^+ signal, as detailed in Hu et al. (2017a) (Figure S3). The CU-AMS data has been corrected for these small effects. The corrections were typically 1% of CO_2^+ and 0.8% Chl.

Three different lens transmission calibrations to characterize the high end of the AMS transmission curve were performed: (1) comparing the NH_4NO_3 mass measured with the CPC and the CU-AMS between 200 – 450 nm (mobility diameter, d_m); (2) comparing the number of particles measured with the CPC and the CU-AMS between 300 – 450 nm (d_m) using the single particle vaporization technique detailed above; and (3) comparing the $(NH_4)_2SO_4$ mass measured with the CPC and the CU-AMS between 250 – 450 nm (d_m), normalizing to the value at 250 nm. The NH_4NO_3 diameters were converted to vacuum aerodynamic diameters (d_{va}), as discussed in DeCarlo et al. (2004). As seen in Figure S4, both techniques show good agreement for the particle transmission, and this transmission is similar to the recommended transmission curve in the literature (Knote et al., 2011; Hu et al., 2017b). For this curve, it is assumed that the transmission linearly increases from 0 – 100% between 40 – 100 nm (d_{va}) (Zhang et al., 2004), remains 100% between 100 – 550 nm (aerodynamic diameter), and decreases linearly from 100 – 0% between 550 nm – 1500 nm (d_{va}). This leads to a 50% cut-off of ~900 nm (d_{va}) during KORUS-AQ.

The particle sizing in the AMS Particle Time-of-Flight (PToF) mode was calibrated with PSLs, ranging from 70 – 700 nm (geometric diameter) (Figure S5). This calibration was compared against the velocities calculated from data collected during the NH_4NO_3 lens transmission measurements. As seen in Figure S5, these two different methods to calibrate the PToF velocity show comparable results, falling within the 95% confidence interval of the PSL calibration. The fact that both PToF calibrations agree, and that the SMPS used for the AN calibrations showed less than 2 nm deviation from the nominal PSLs diameters at all sizes increases our confidence in accuracy of the IE calibration described above, and in particular on lack of evaporation of NH_4NO_3 after its size selection in the DMA.

Finally, the vaporizer power, and thus, temperature, was calibrated by using monodisperse $NaNO_3$ particles of d_m = 350 nm (Figure S8), as recommended by Williams (2010) and Hu et al. (2017b). This method is more accurate than relying on the temperature reported by the thermocouple on the AMS vaporizer, which can often be unreliable (Williams, 2010; Hu et al., 2017b). The general idea is to increase the vaporizer power between ~1 – 7 W and locate where the $NaNO_3$ full-width half maximum nearly remains constant, indicating that the vaporizer temperature is ~600°C and allowing for maximum peaks in OA, pNO_3, and SO_4 while minimizing the influence of refractory species (Williams, 2010; Hu et al., 2017b).

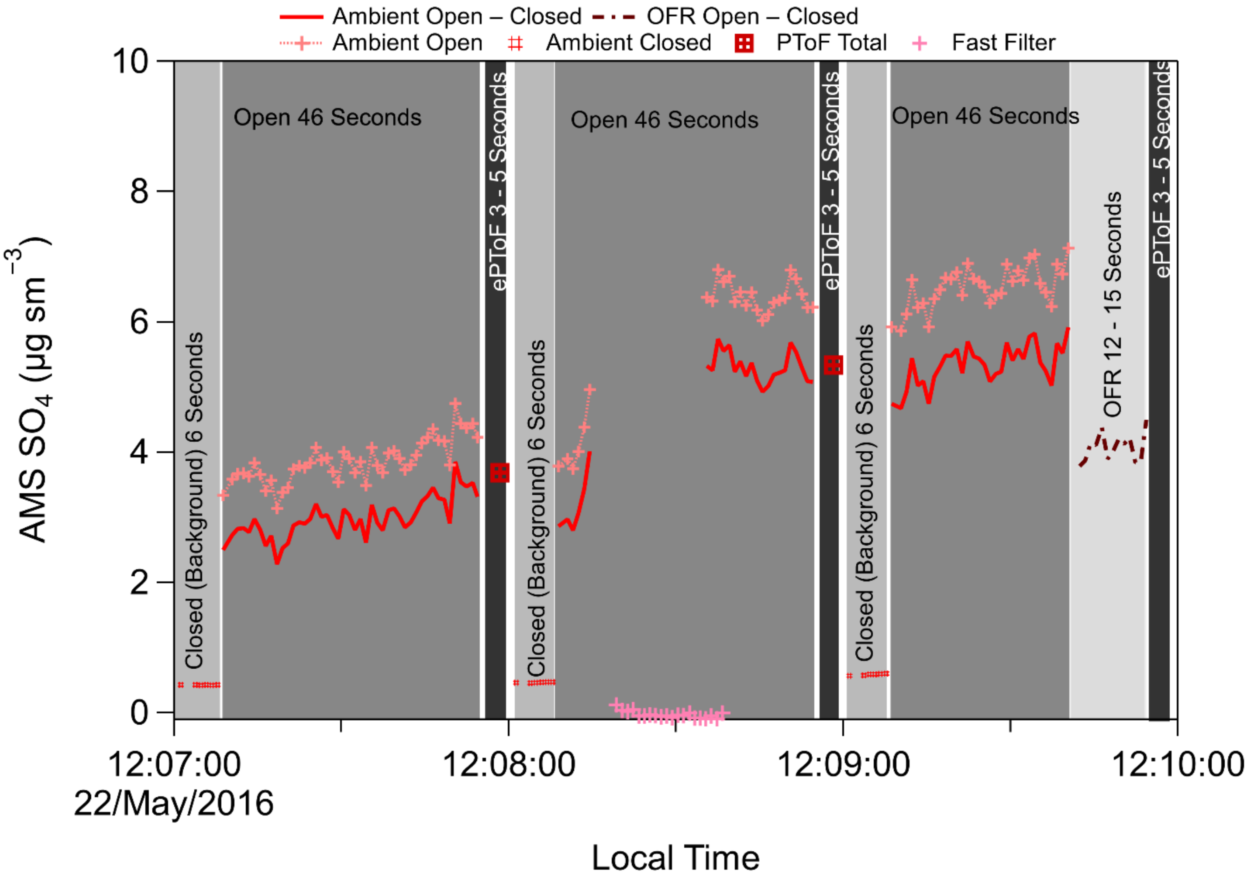

Figure S2. Example time series of the CU-AMS sampling scheme during KORUS-AQ. Though the final 8 s of each minute are dedicated to ePToF, some of the time is ued by the computer in saving the 6 s of closed and 46 s of open signal and ePToF signal; therefore, only 3 – 5 s of ePToF signal is actually recorded. The approximate saving time are shown as white spaces.

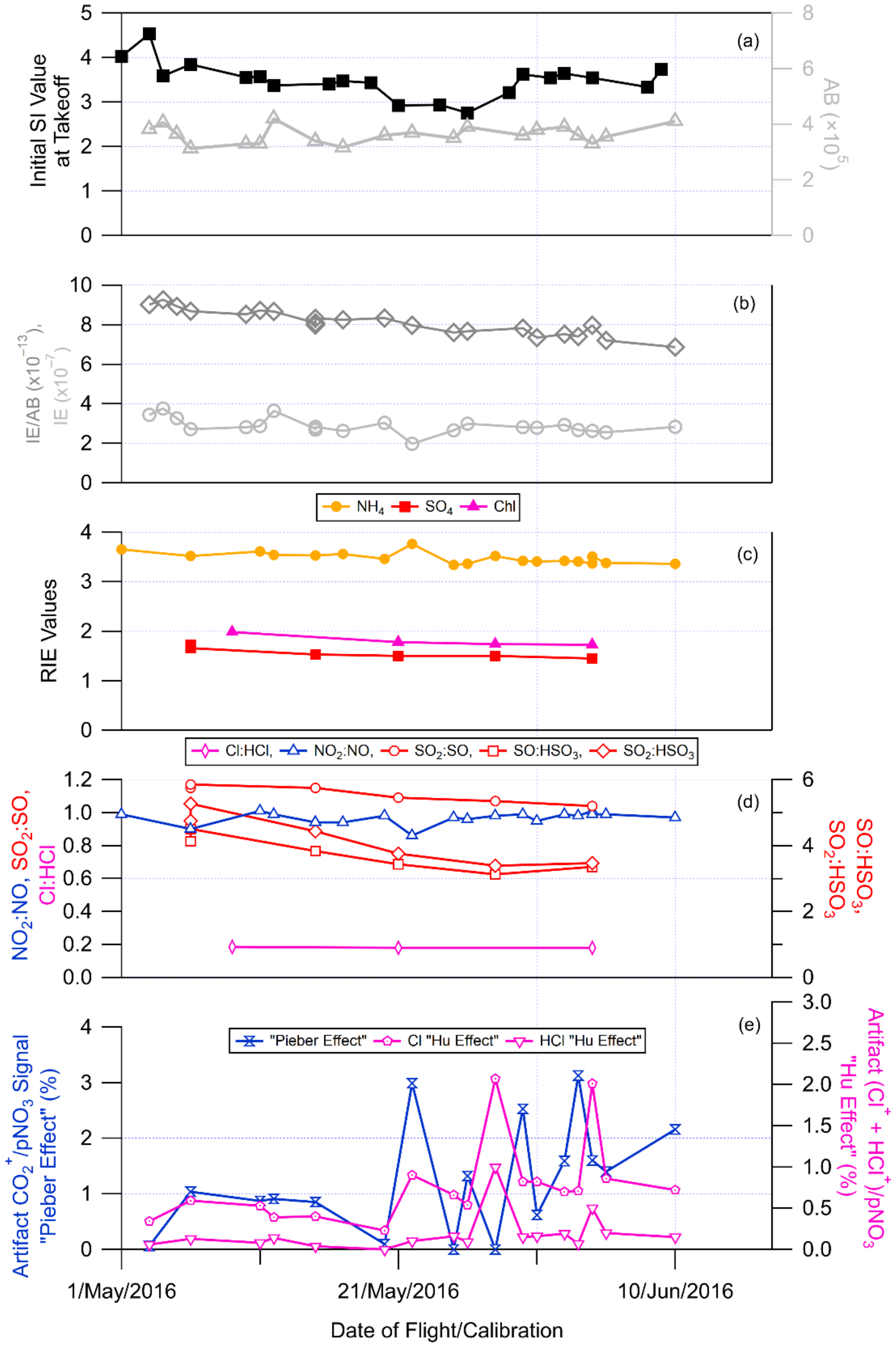

Figure S3. Time series of the (a) the Single Ion (SI) at take-off for each flight; (b) the air beam (AB, dark grey), ionization energy (IE, light grey), and IE/AB (middle grey) for each calibration; (c) the relative ionization energies (RIE) for ammonium (NH_4), sulfate (SO_4), and chloride (Chl) for each calibration; (d) the ratios of different ions for each calibration; and, (e) measured artifact signal ratios for CO_2^+/pNO_3 “Pieber effect” (Pieber et al., 2016) and $(Cl^+ + HCl^+)/pNO_3$ “Hu efffect” (Hu et al., 2017a) effects from each calibration.

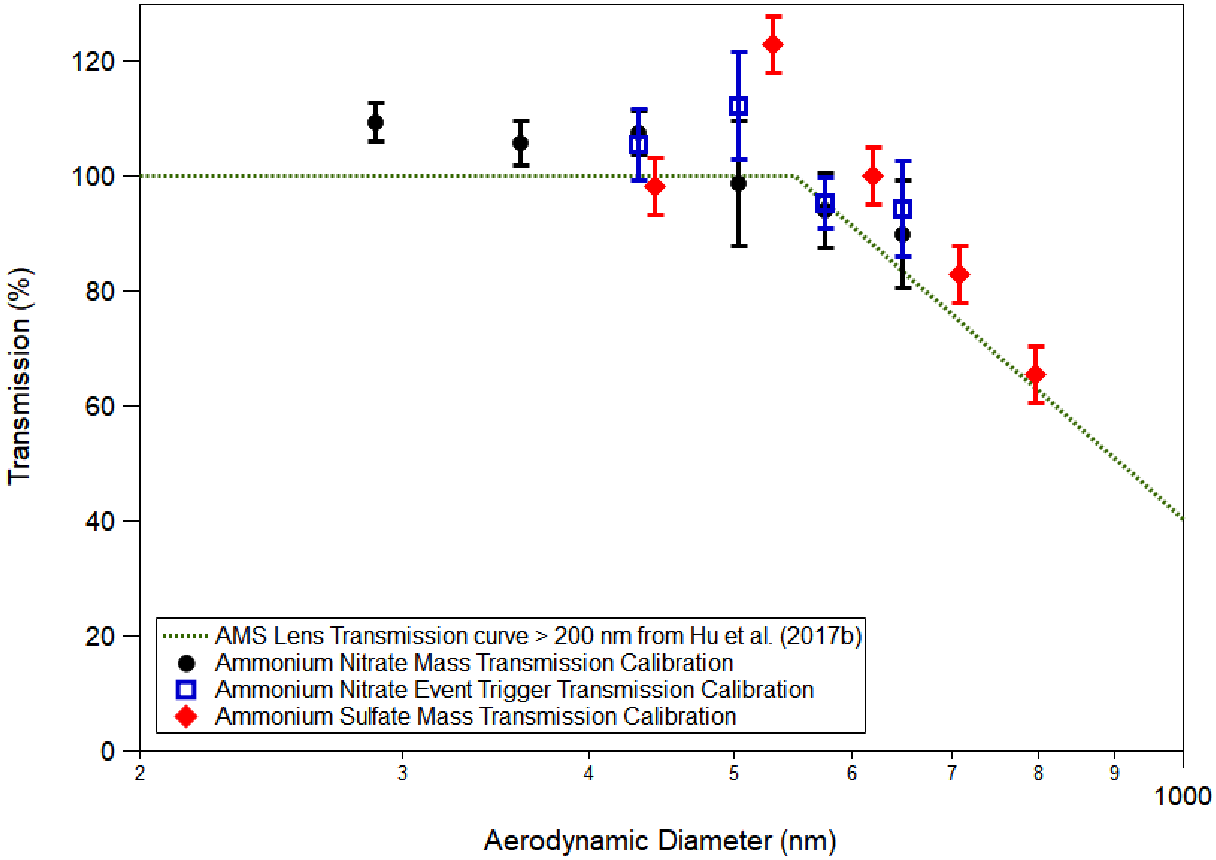

Figure S4. Measured transmission percentage of ammonium nitrate and ammonium sulfate versus vacuum aerodynamic diameters (nm) during KORUS-AQ. The green dashed-line is the expected transmission curve for the CU-AMS from the literature (Knote et al., 2011; Hu et al., 2017b). The black data represents the ammonium nitrate transmission curve using mass closure, from an experiment conducted on 09/May/2016. The blue data represents the ammonium nitrate transmission curve using single particle ("event trigger") number closure, from an experiment conducted on 17May/2016. The red data represents the ammonium sulfate transmission curve using mass, from an experiment conducted on 06/May/2016. Finally, the error bars represent 1σ variability for the transmission at each size.

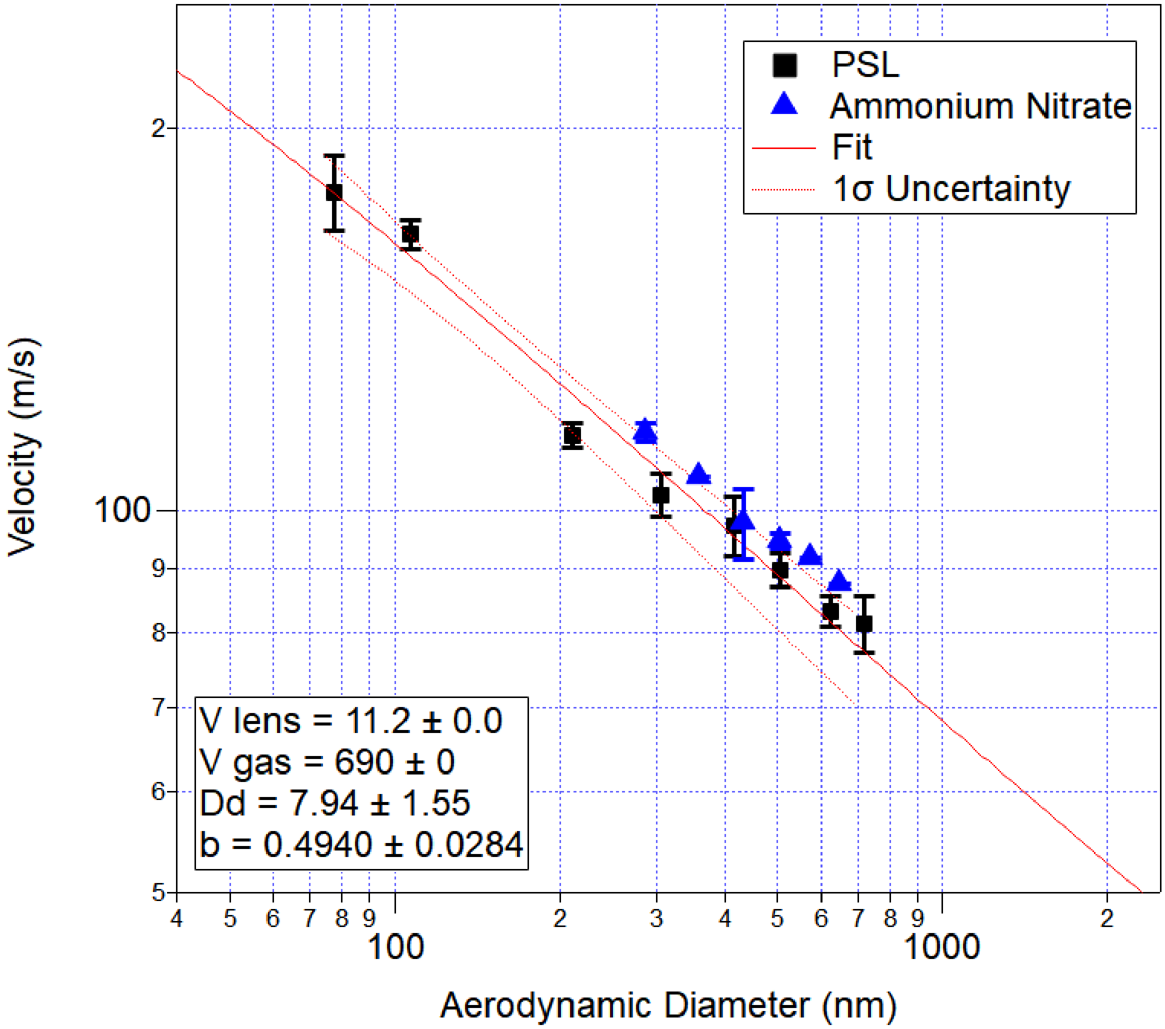

Figure S5. Particle velocity (m/s) inside the AMS vacuum chamber (after exiting the aerodynamic lens) versus vacuum aerodynamic diameter (nm) calibrations for the ePToF mode, using PSLs (black). Solid red line is the fit to the PSLs. The ammonium nitrate measured for the mass closure transmission curves (Figure S4) for comparison to the PSL values.

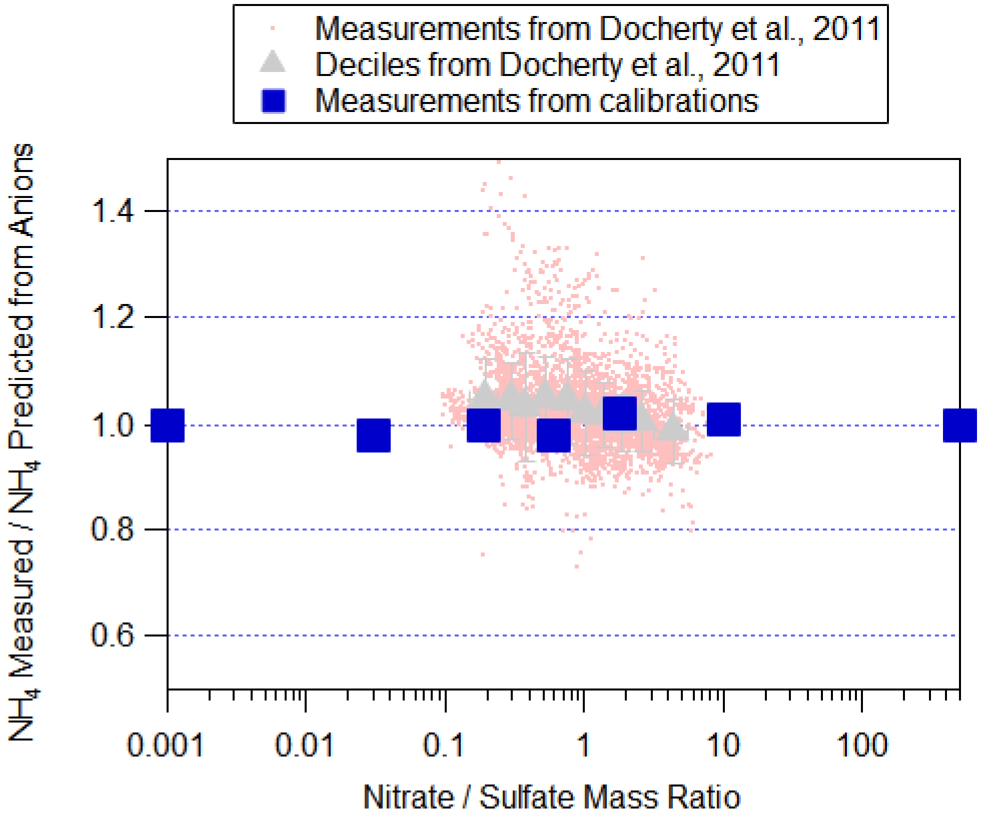

Figure S6. Ratio of measured and predicted NH_4 from anions versus ratio of nitrate to sulfate mass. Red points are from Docherty et al. (2011), grey triangles are deciles of the data from Docherty et al., and blue points are measurements from calibration solutions of varying mixtures of NH_4NO_3 and $(NH_4)_2SO_4$. Such consistency would be unexpected if a major fraction of the particle NH_4^+ evaporated as intact salts, as suggested by Murphy (2016) (Hu et al., 2017b) .

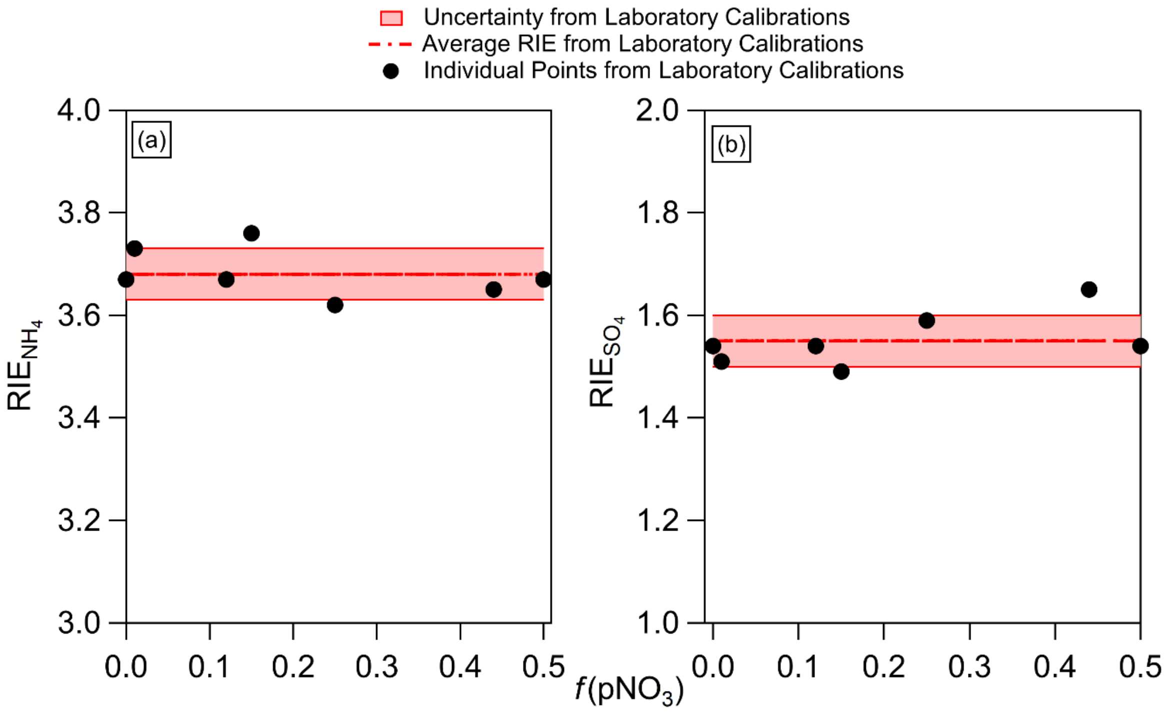

Figure S7. (a) Plot of NH_4 RIE, keeping SO_4 RIE constant, versus the molar fraction of pNO_3 measured in the solution, for calibration solutions of varying mixtures of NH_4NO_3 and $(NH_4)_2SO_4$. (b) Same as (a), but for SO_4 RIE and keeping NH_4 RIE constant. For both figures, the black dots are the values from the calibrations, the thick red line is the average of all the values, and the shaded red area is ±1σ.

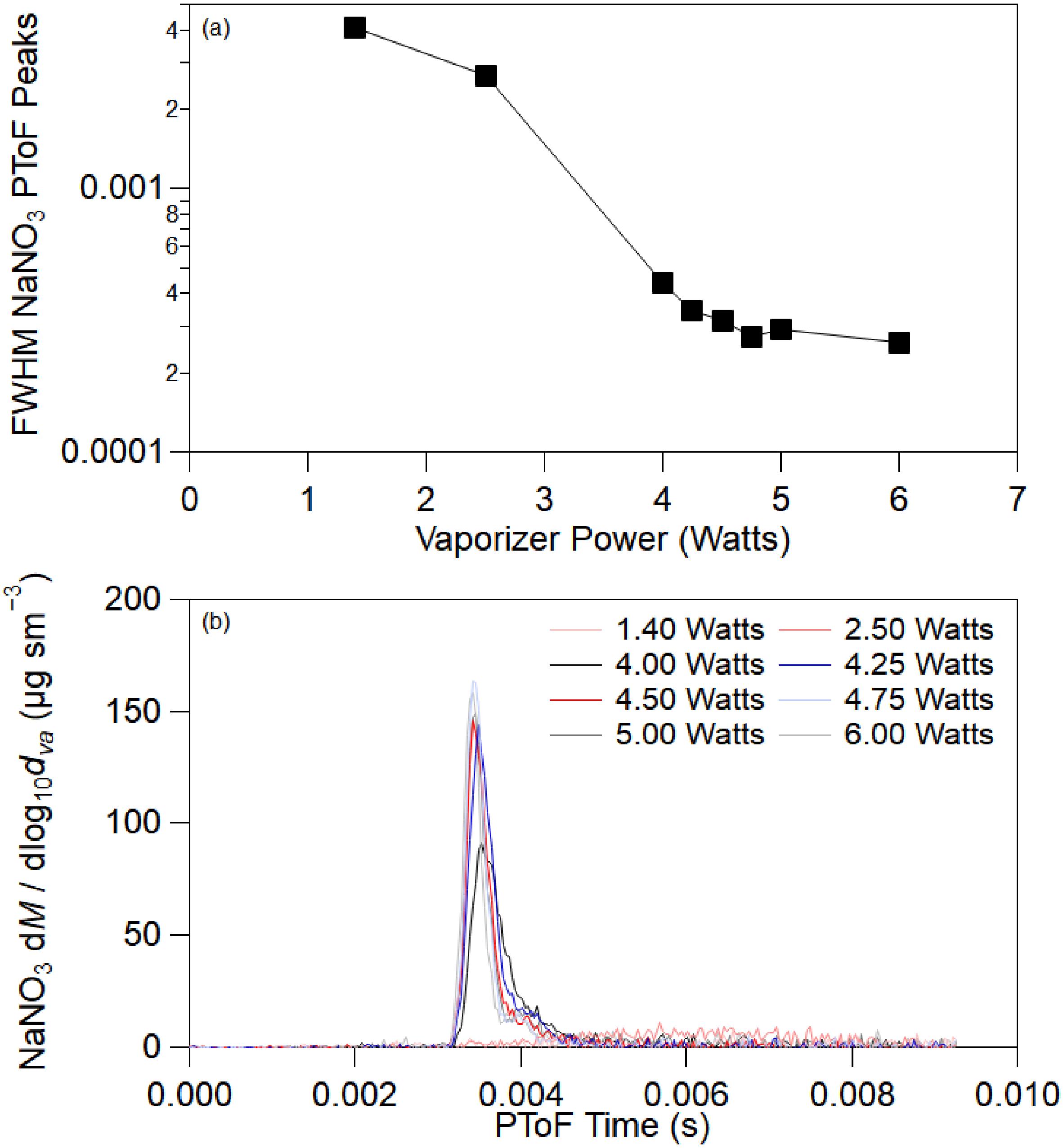

Figure S8. (a) Full-width half-maximum (FWHM) of NaNO$_3$ size distributions in PToF mode (b) vs. different vaporizer power inputs. See text for further details.

S3. Application of Positive Matrix Factorization (PMF)

Positive matrix factorization analysis (PMF, performed using the CU-Boulder PMF Evaluation Tool PET-Panel v3.00A, http://cires1.colorado.edu/jimenez-group/wiki/index.php/PMF-AMS_Analysis_Guide#PMF_Evaluation_Tool_Software) (Ulbrich et al., 2009) was used to apportion the total OA aerosol into several components. PMF was run on the combined CU-AMS 1 min organic ion matrix for all RFs together during KORUS-AQ. A 6-factor solution was derived with an FPEAK value of 0. Based on comparisons with reference mass spectra from the AMS high-resolution spectral database (http://cires1.colorado.edu/jimenez-group/HRAMSsd/#Ambient), comparisons of time series (Figure S9), and correlations with other trace species (Figure S11), the factors were recombined into more-oxidized, oxidized organic aerosol (MO-OOA), less-oxidized, oxidized aerosol (LO-OOA), and hydrocarbon-like organic aerosol (HOA) (Figure S10). HOA correlated with primary emissions (e.g., NO_x, various hydrocarbons) whereas LO-OOA and MO-OOA correlated with secondary photochemical products (e.g., CH_2O, PAN, pNO_3, SO_4). Here, primary OA is defined as the HOA factor and total oxidized OA (OOA) as the LO-OOA plus MO-OOA factors. OOA is assumed to be dominantly composed of secondary organic aerosol, which is supported by its strong correlation with other secondary photochemical products as documented in the paper, as well as by many prior studies (e.g., Jimenez et al., 2009; and references therein).

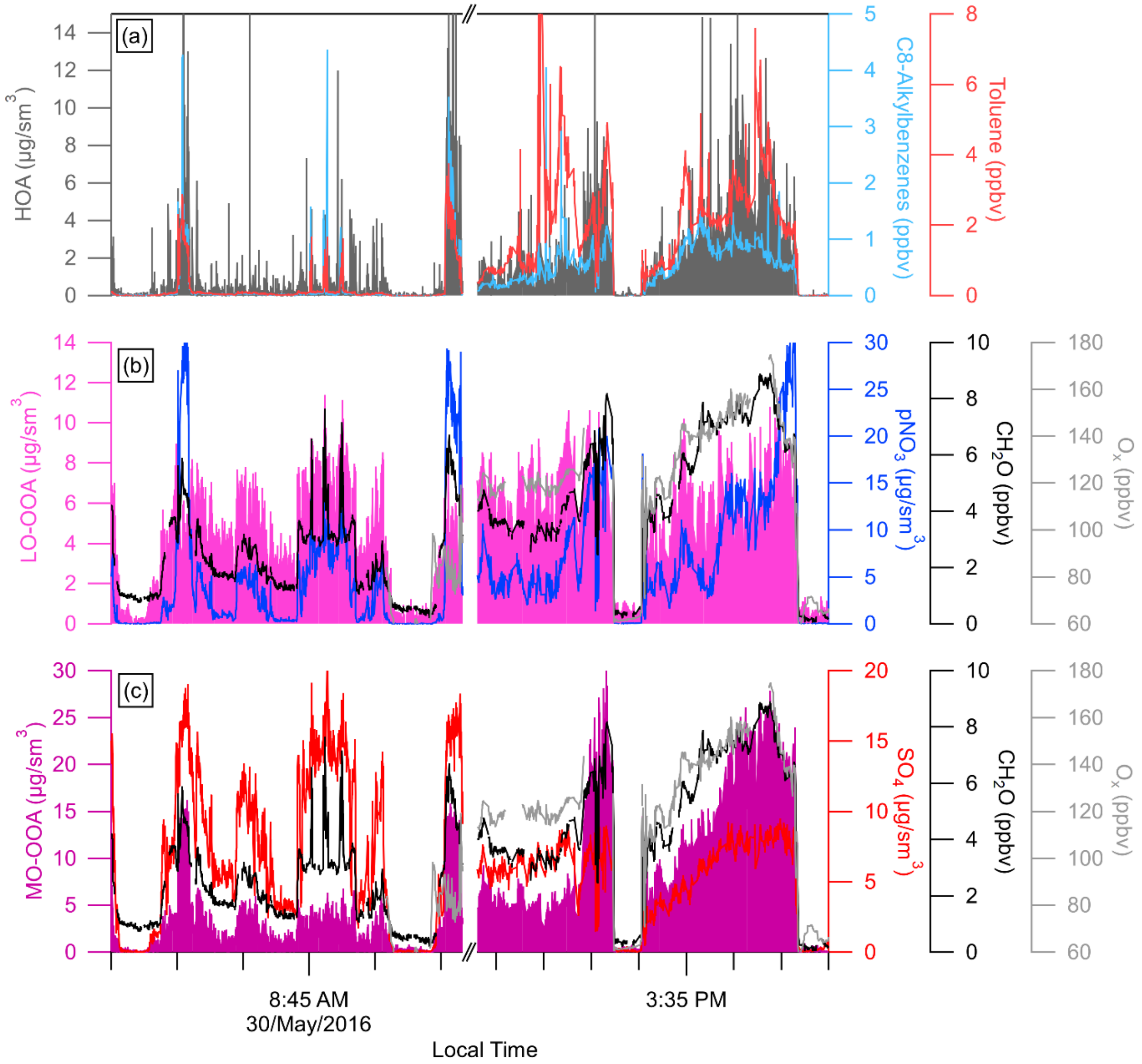

Figure S9. Example time series of the 3 PMF ((a) HOA, (b) LO-OOA, and (c) MO-OOA) results (left axes) and some species that correlate with the corresponding PMF results (right axes) from RF14. The morning and afternoon overpasses over Seoul, South Korea, are shown.

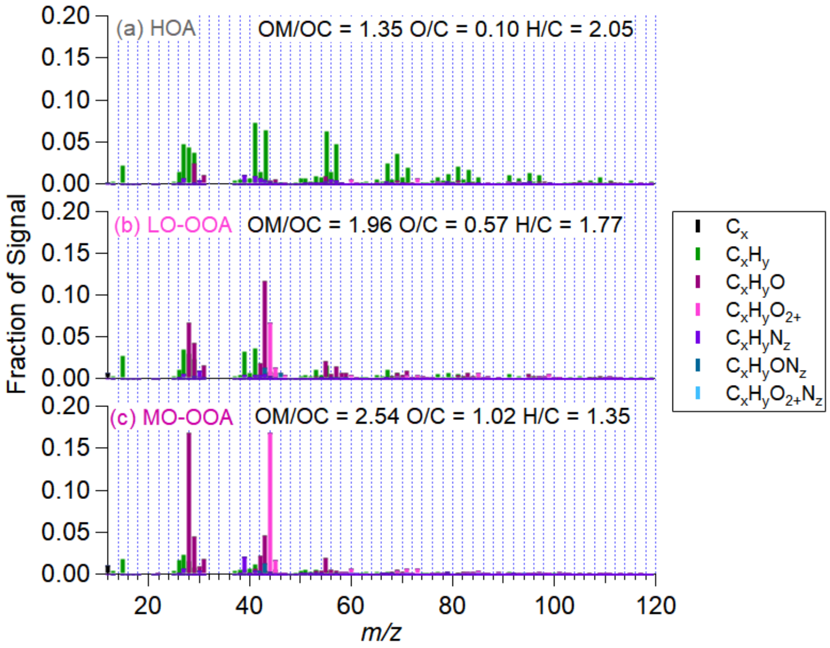

Figure S10. Mass spectra for PMF solution (a) HOA, (b) LO-OOA, and (c) MO-OOA for all of KORUS-AQ.

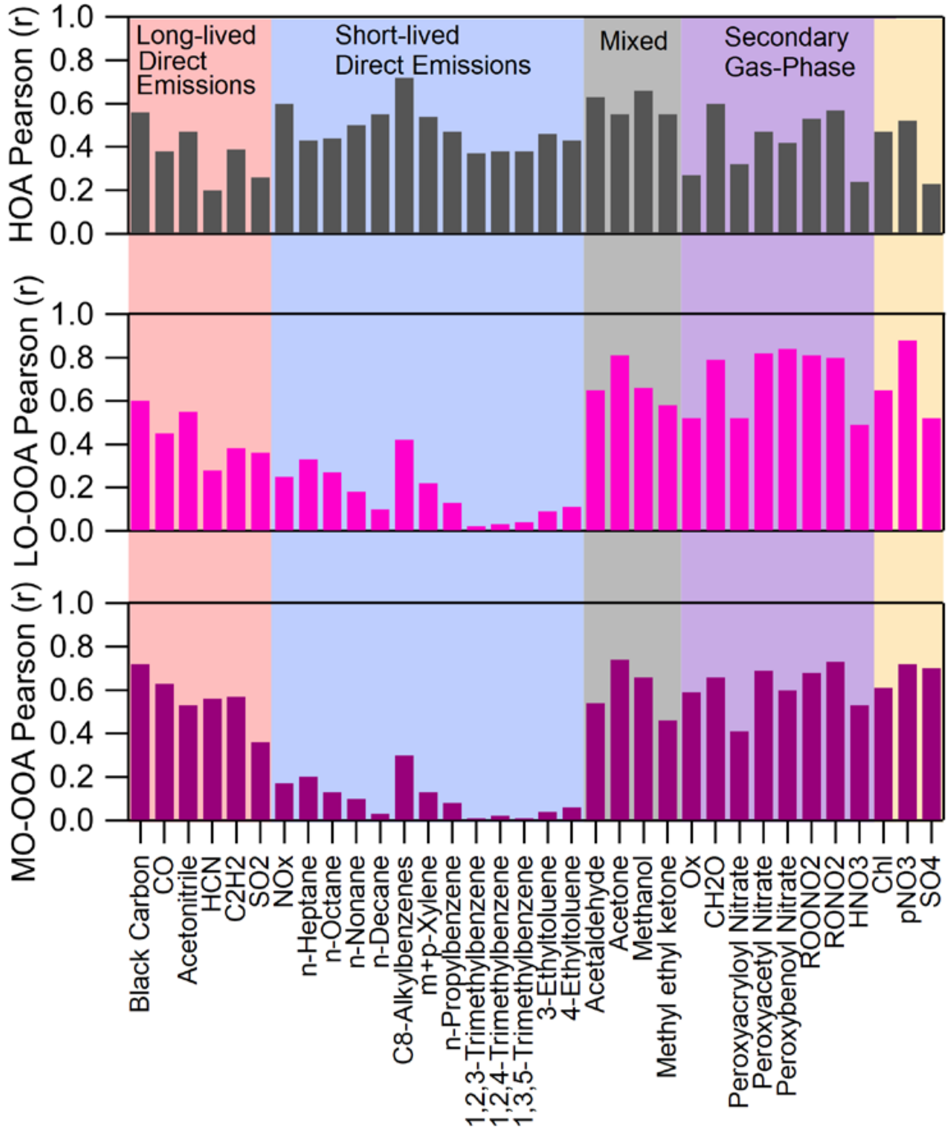

Figure S11. Pearson correlation coefficients for HOA (grey, top), LO-OOA (light pink, middle), and MO-OOA (dark pink, bottom) factors versus species listed in x-axis. The background colors represent the dominant group of sources of the correlating species. The yellow in the far right indicates other PM_1 components measured by the CU-AMS.

S4. Oxidation Flow Reactor (OFR) Sampling

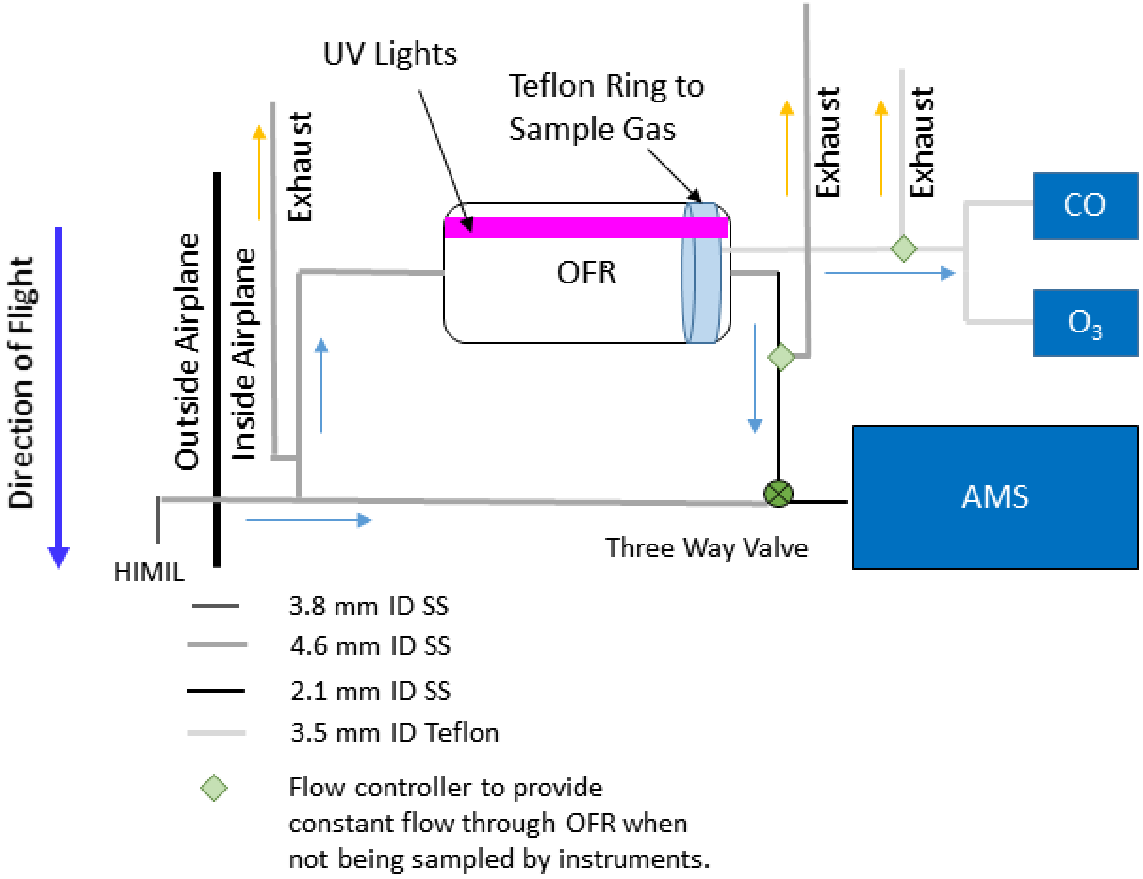

Figure S12. Schematic of the OFR sampling during KORUS-AQ. UV lamp is represented by the purple light in the OFR. Size and type of tubing is represented in figure, where ID is internal diameter and SS is stainless steel. Tubing distances were always as short as feasible and often shorter than represented, but they are stretched in this drawing for clarity

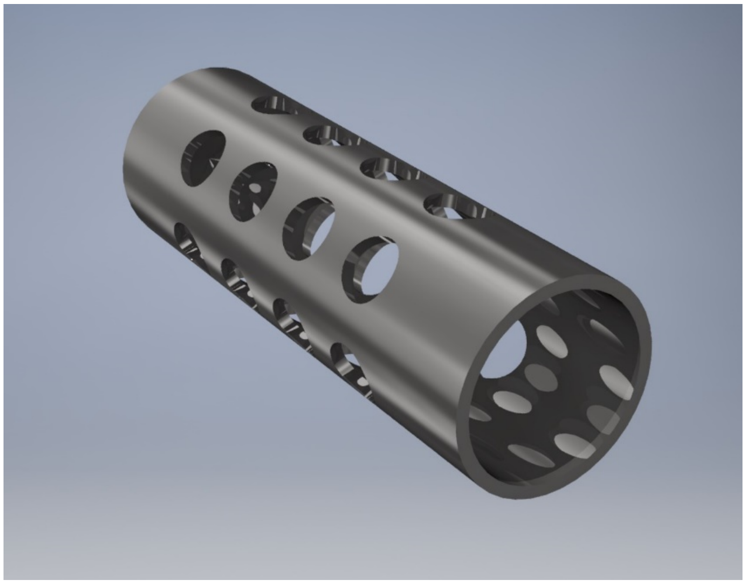

Figure S13. 3D rendition of the computer model of the ½” press fitted stainless steel inlet, coated in SilcoNert (SilcoTek Co, Bellefonte, PA), used in the inlet of the OFR during KORUS-AQ, to avoid “short-circuiting” between the inlet and outlet of the OFR.

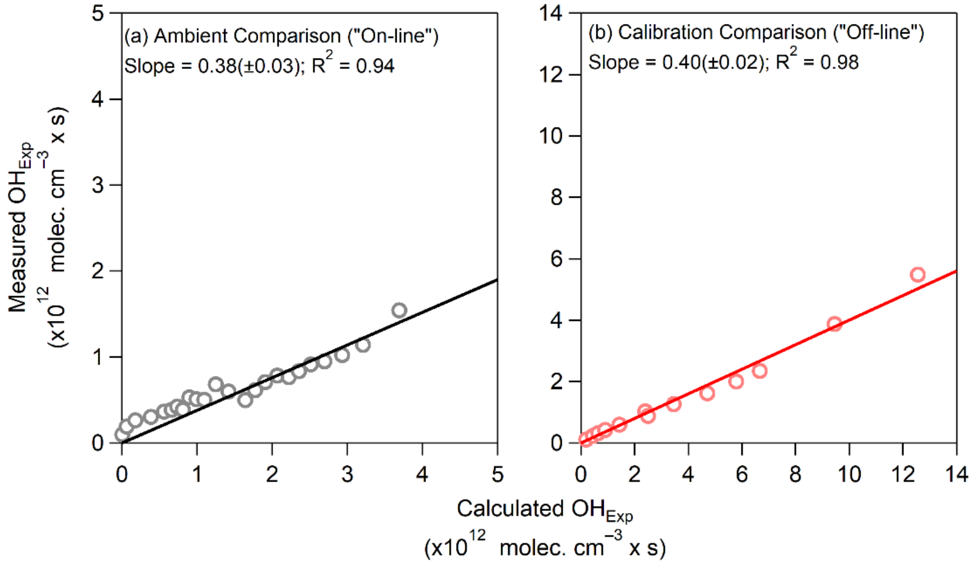

Figure S14. (left) Measured OH_{exp} from the decay of CO in ambient air (measured by the DACOM instrument, see text) and OFR output air (measured by the Picarro instrument) and (right) measured OH_{exp} from the decay of CO from a calibration cylinder versus calculated OH_{exp} using the predictive expression in Peng et al. (2015). The calibration factor determined by this analysis was similar to past studies (Palm et al., 2016) and was applied to all data shown in this paper.

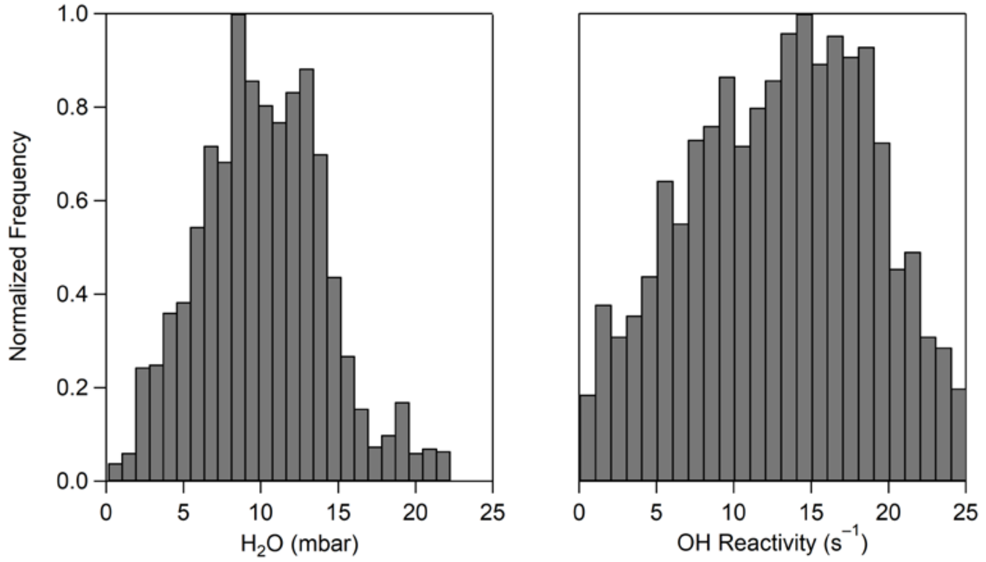

Figure S15. (left) Frequency distribution of water vapor below 2 km during KORUS-AQ. (right) Normalized histogram of measured OH reactivity (OHR) below 2 km during KORUS-AQ.

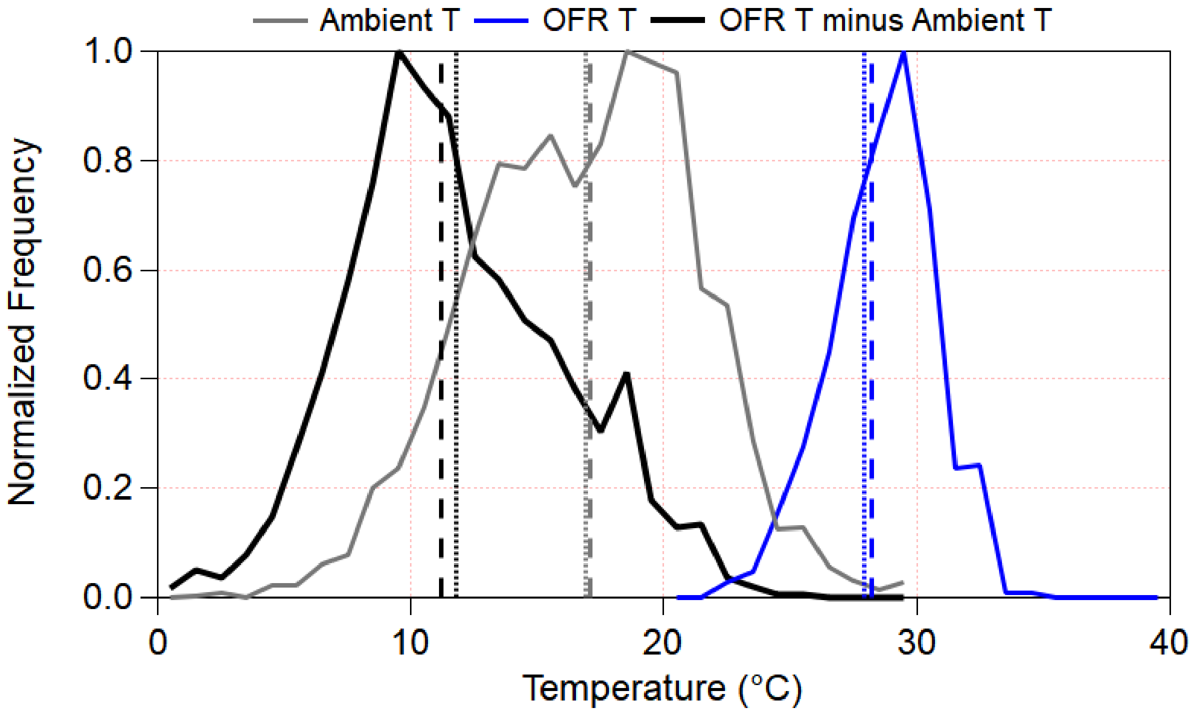

Figure S16. Frequency distribution of the ambient (black), OFR (blue), and difference between OFR and ambient temperature (grey) (°C). Vertical lines show the mean (long-dashed) and median (short-dashed) temperatures for the ambient, OFR, and difference between the two.

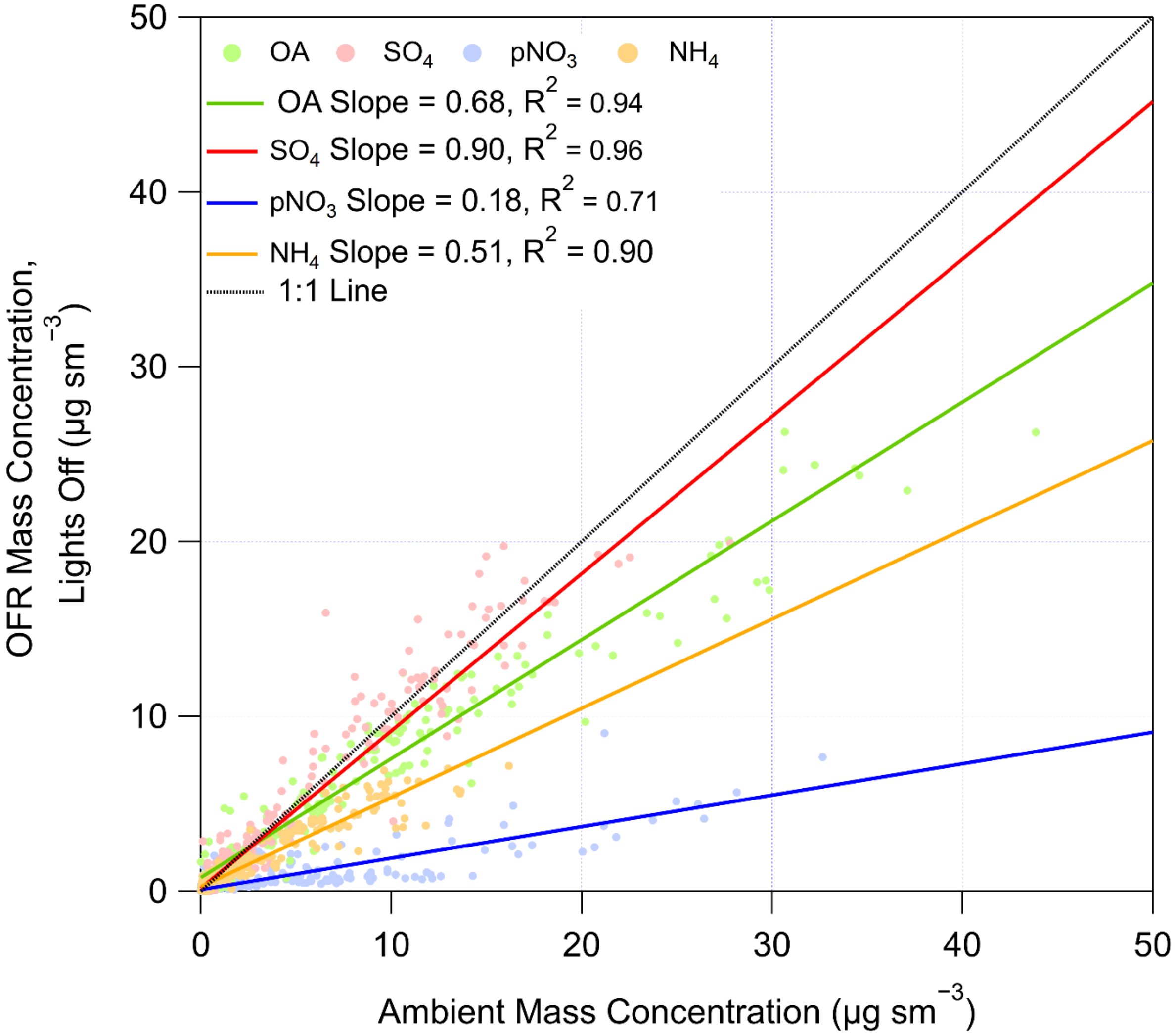

Figure S17. Comparison of organic (green), sulfate (red), nitrate (blue), and ammonium (orange) aerosol sampled through the OFR, with lights off, versus ambient aerosol. Under these conditions the OFR is just acting as a thermal denuder (e.g. Huffman et al., 2009), leading to evaporation of some aerosols due to increased temperature in the aircraft cabin vs. outside. In addition, small particle losses in lines and the OFR are observed for sulfate, which is generally non-volatile. See text for further details and discussion.

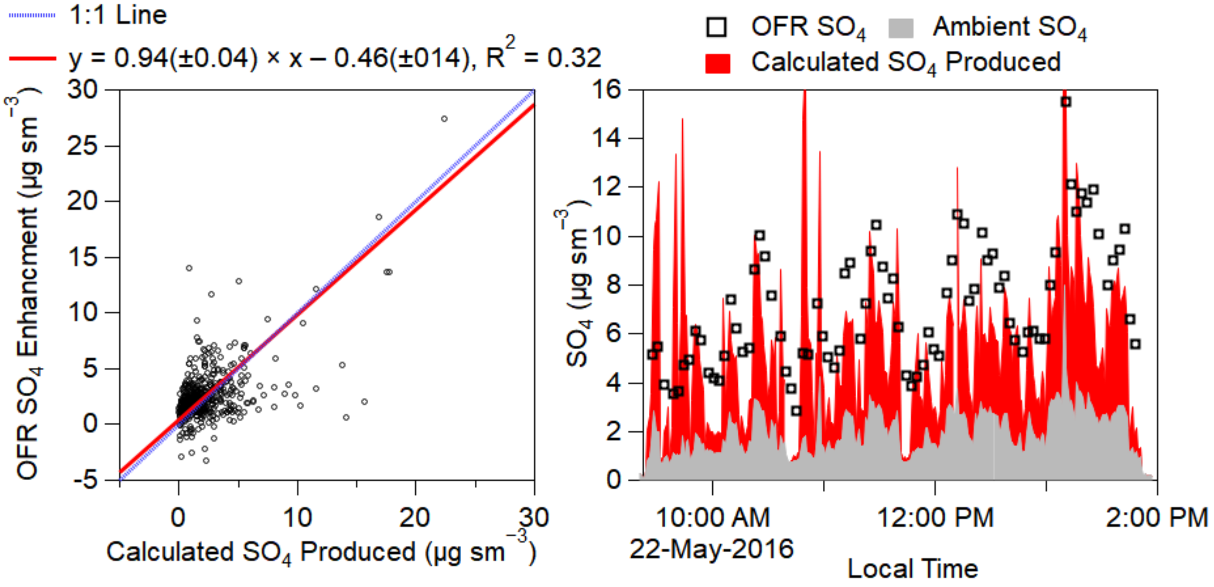

Figure S18. (a) Scatter plot of OFR SO_4 Enhancement (OFR – Ambient) versus calculated SO_4 produced, using SO_2 observations, estimated OH_{exp}, and condensation fate correction. (b) Time series of OFR SO_4 (black squares), ambient SO_4 (light grey), and calculated SO_4 (dark red) for the RF11 flight.

Analysis of CS Values for KORUS-AQ

If we used the condensational sink from just the ambient data, which neglects the added particle surface area formed in the OFR as described in Section 2.4 and Eq. 1 (Ortega et al., 2016; Palm et al., 2016, 2017, 2018), the agreement between calculated and measured SO_4 enhancement decreases to a slope of 0.74 (R^2 = 0.28), indicating that the condensational sink is likely too low. This suggests that, to first order, the aerosol surface area, estimated from observations and Eq. 1 (in the main paper), provides a reasonable estimate of the condensational sink within the OFR during KORUS-AQ. Thus, similar to other studies (Ortega et al., 2016; Palm et al., 2016, 2017, 2018), we find, at the typical OH_{exp} in the OFR, that 50 – 60% of the oxidized condensable organic gases are condensing onto aerosol, with 20 – 25% undergoing further reactions with OH leading to highly volatile compounds, 8 – 13% exiting the OFR prior to condensing on aerosol, and 12%

condensing to the wall (Figure S19). Note that the further reactions with OH are not relevant for H_2SO_4, and thus they have not been included in the analysis shown in in Fig. SI-18.

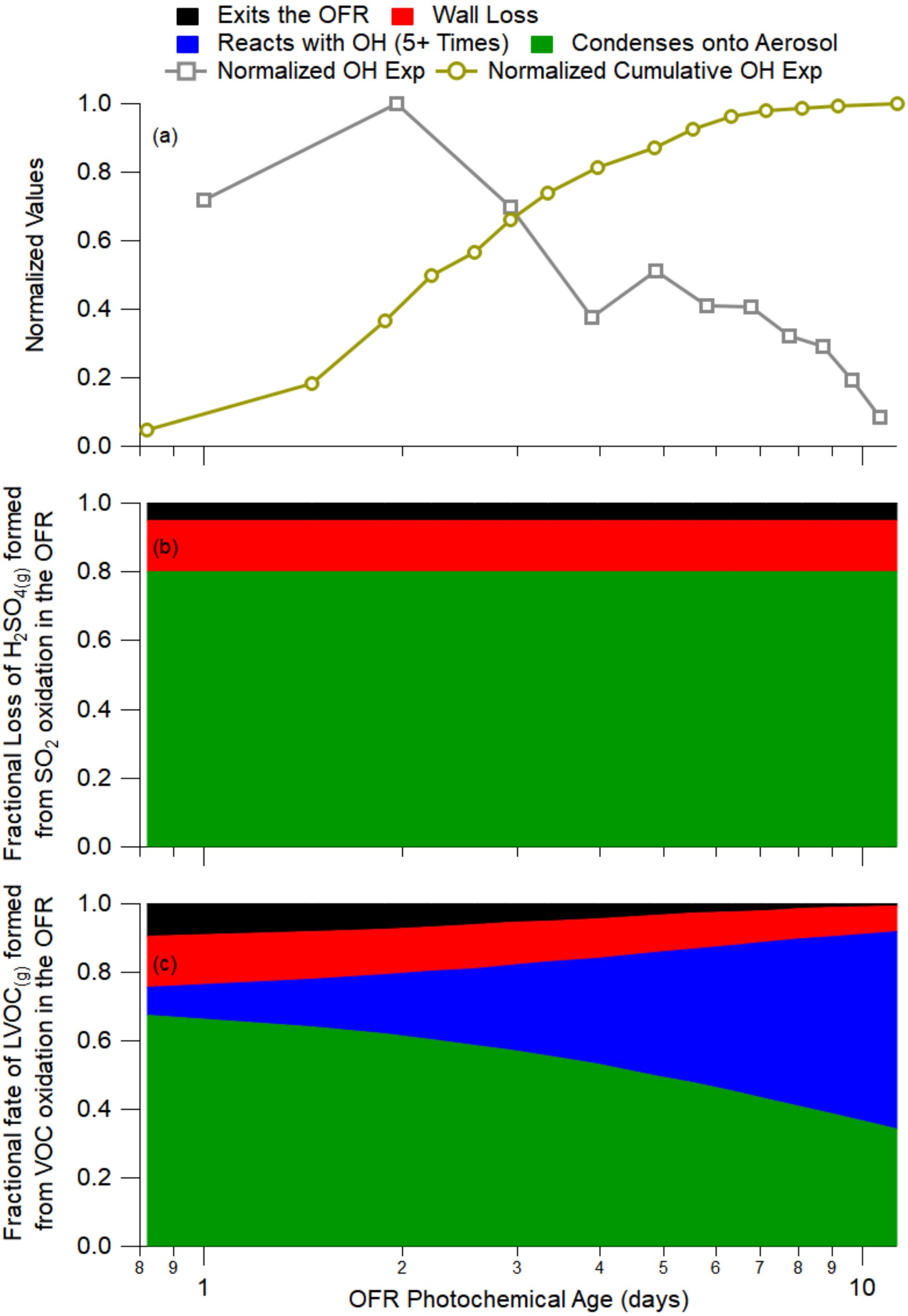

Figure S19. (a) Observed normalized frequency and cumulative frequency of OH Exposure observed during KORUS-AQ in the OFR. (b) Calculated fate of the SO_2 oxidized in the OFR versus OFR OH Exposure. (c) Calculated fate of low-volatility condensable vapors (formed from VOC oxidation) versus OFR OH Exposure. For (b) and (c), the losses include flowing through the OFR without condensing onto aerosol (black), condensing onto the wall (red), condensing onto the aerosol (assuming a median value of 85.8 s, green), and reacting with OH enough to make it too volatile to condense onto aerosol (blue).

S5. Calculation of Photochemical Age over Seoul, South Korea

The photochemical clock calculations used throughout this work are described here. The rate constants used for these clocks are located in SI Table 3. For the NO_x/NO_y photochemical clock (e.g., Kleinman et al., 2007) (herein referred to as the NO_x photochemical clock), Eq. S1 is used, with the updated rate constant from Mollner et al. (2010).

$$t = \frac{ln\left(\frac{NO_x}{NO_y}\right)}{k_{OH+NO_2}[OH]} \tag{S1}$$

where *t* is the time, in days, [OH] is assumed to be 1.5×10^6 molecules/cm^3 (for standarization), and NO_x and NO_y are the chemiluminescence measurements. The NO_x clock is used for photochemical ages less than 1 day to (1) reduce the effect of loss of HNO_3 and other oxidized reservoirs due to deposition (lifetime ~6 hours) (Neuman et al., 2004; Nguyen et al., 2015; Romer et al., 2016) and (2) to ensure that t was still sensitive (and precise) to the NO_x and NO_y concentrations (~20% of NO_x still remaining at $t = 1$ day).

For the aromatic photochemical clock over Seoul, the more reactive aromatics (ethylbenzene in the denominator) are utilized, which should be more sensitive to the short photochemical aging observed over Seoul (Parrish et al., 2007), along with Eq. SS2.

$$t = -\frac{1}{[OH]\times\left(k_{aromatic_i} - k_{ethylbenzene}\right)} \times \left(ln\left(\frac{aromatic_i(t)}{ethylbenzene(t)}\right) - ln\left(\frac{aromatic_i(0)}{ethylbenzene(0)}\right)\right) \tag{S2}$$

where *t* is the time, in hours, the *k*'s are the corresponding OH rate constants for each aromatic compound (SI Table 3), and the third term (ln $\left(\frac{\text{aromatic}_i(0)}{\text{ethylbenzene}(0)}\right)$) corresponds to the emission ratios for those two aromatic compounds. Similar to the NO_x clock, we assume $[OH] = 1.5\times10^6$ molecules/cm^3 for standardization. The aromatics measurements used in this calculation are from WAS.

To evaluate which aromatic compounds to use in the clock, the behavior of the ratios of each aromatic compound with ethylbenzene versus the three missed approaches (morning, noon, and afternoon) over Seoul during KORUS-AQ (Figure S20) are compared. The idea is that if the 2 aromatic compounds are co-emitted, the ratios should be removed proportionally to their OH rate constants. E.g. for faster reacting compounds (e.g., o-xylene), the ratio to ethylbenzene should decrease with time as more o-xylene was consumed, compared to ethylbenzene, by OH (de Gouw et al., 2017). On the other hand, for slower reacting compounds (e.g., toluene), the ratio to ethylbenzene should increase with time as more ethylbenzene was consumed by OH. Also, this analysis provides an indication of which ratios would provide meaningful results throughout the entire day (de Gouw et al., 2017). Ideally, there should be a decrease with each later missed approach, and not a leveling off after two missed approaches (e.g., the trimethylbenzenes and ethyltoluenes). Only the m+p-xylene/ethylbenzene and o-xylene/ethylbenzene ratios meet this criterion. Finally, to determine the emission ratios, we calculated what the m+p-xylene/ethylbenzene and o-xylene/ethylbenzene ratio was for observations where the NO_x photochemical was less than 0.07 days (corresponding to less than 10% of either species being consumed). Comparing these two aromatic clocks to the NO_x photochemical clock (Figure S21), a similar agreement between the two aromatic clocks with the NO_x photochemical clock was observed, providing confidence in using all three clocks to calculate photochemical age to evaluate OA production over Seoul. For the remainder of the paper, we mainly use the NO_x photochemical clock to eliminate the uncertainty of the emission ratios, unless otherwise noted.

Finally, for observations over the Yellow Sea, the aromatic clock (Eq. SS2) was used, but benzene and toluene were used since these air masses are more photochemically processed (Parrish et al., 2007). For the emission ratios, values reported by Yuan et al (2013) were used.

303

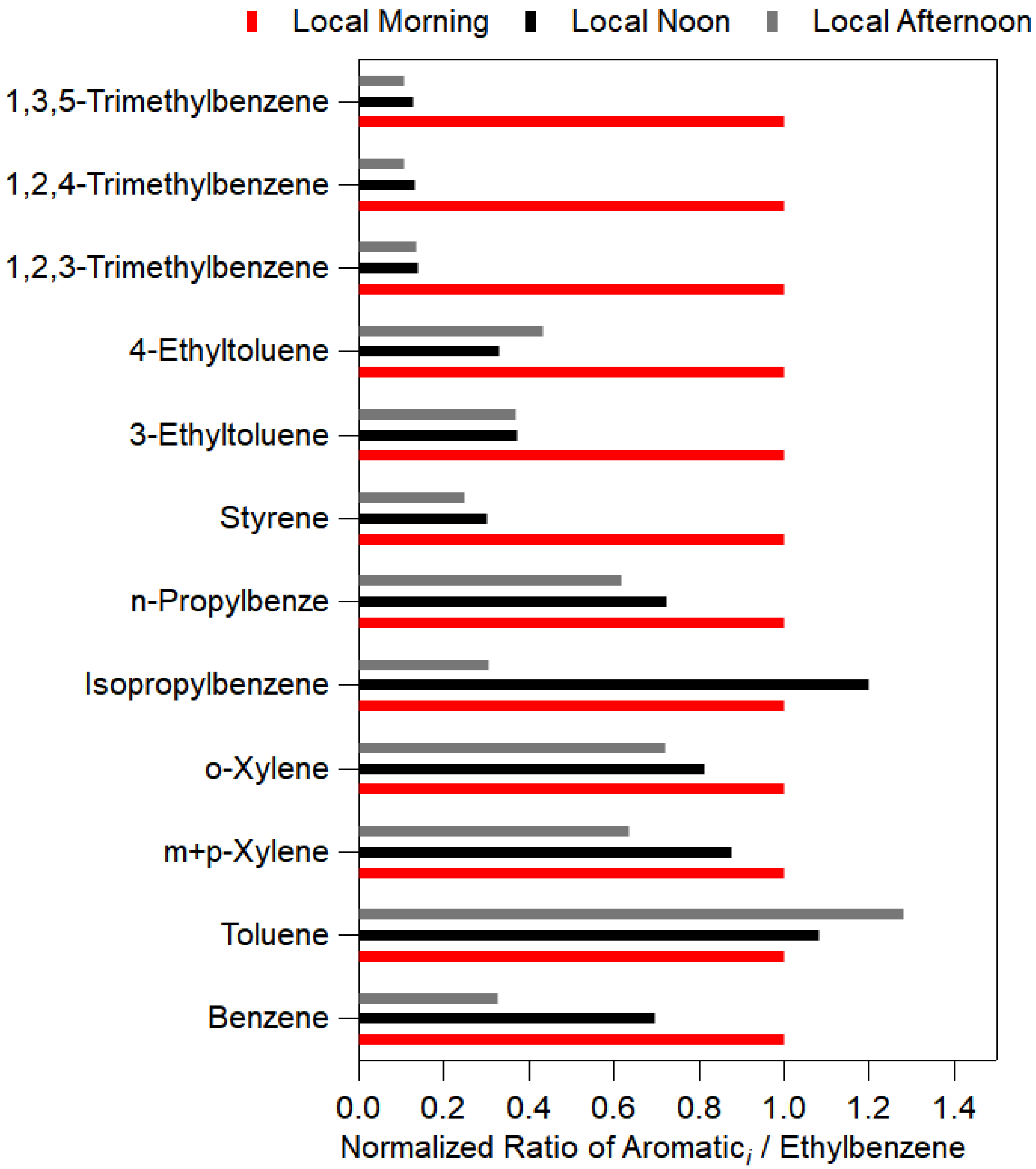

304

305 **Figure S20.** Comparison of various aromatic compounds/ethylbenzene ratios sampled over Seoul,
306 South Korea, during KORUS-AQ. The ratios are normalized by the morning ratios.

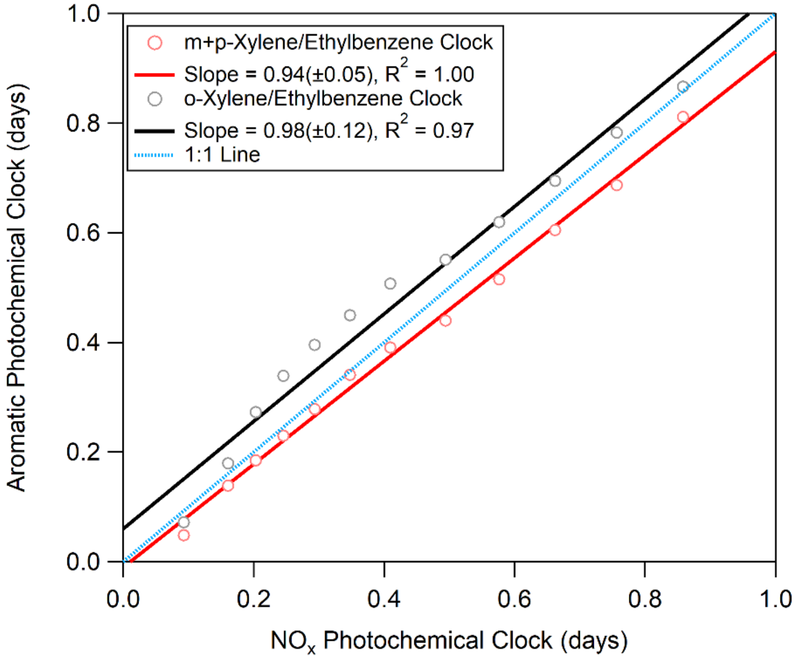

Figure S21. Binned scatter plot of the aromatic photochemical clock ages versus NO_x photochemical clock ages for all observations over Seoul. All ages are normalized to OH = 1.5×10^6 molecules/cm^3.

Table S3. Rate constants used throughout this study. Unless noted otherwise, rate constants without temperature dependence only have a value measured at 298 K.

Reaction	Rate Constant (cm^3/molecules/s)	Reference
Inorganic		
CO	$2.28\times10^{-13,a}$	Sander et al. (2011)
NO_2	$1.23\times10^{-11,a}$	Mollner et al. (2010)
SO_2	$8.94\times10^{-13,a}$	Atkinson et al. (2004)
Alkanes		
Ethane	$6.9\times10^{-12}\times\exp(-1000/T)$	Atkinson et al. (2006)
Propane	$7.6\times10^{-12}\times\exp(-585/T)$	Atkinson et al. (2006)
n-Butane	$9.8\times10^{-12}\times\exp(-425/T)$	Atkinson et al. (2006)
i-Butane	$1.17\times10^{-17}\times T^2\times\exp(213/T)$	Atkinson (2003)
n-Pentane	$2.52\times10^{-17}\times T^2\times\exp(158/T)$	Atkinson (2003)
i-Pentane	3.6×10^{-12}	Atkinson (2003)
n-Hexane	$2.54\times10^{-14}\times T\times\exp(-112/T)$	Atkinson (2003)
Methyl-cyclopentane	7.65×10^{-12}	Sprengnether et al. (2009)
Cyclohexane	$3.26\times10^{-17}\times T^2\times\exp(262/T)$	Atkinson (2003)
Methyl-cyclohexane	9.43×10^{-12}	Sprengnether et al. (2009)
n-Heptane	$1.95\times10^{-17}\times T^2\times\exp(406/T)$	Atkinson (2003)
n-Octane	$2.72\times10^{-17}\times T^2\times\exp(361/T)$	Atkinson (2003)
n-Nonane	$2.53\times10^{-17}\times T^2\times\exp(436/T)$	Atkinson (2003)
n-Decane	$3.17\times10^{-17}\times T^2\times\exp(406/T)$	Atkinson (2003)
Alkenes		
Ethylene	$7.84\times10^{-12,a}$	Atkinson et al. (2006)
Propene	$2.86\times10^{-11,a}$	Atkinson et al. (2006)
1-butene	$6.6\times10^{-12}\times\exp(465/T)$	Atkinson et al. (2006)
i-butene	$9.4\times10^{-12}\times\exp(505/T)$	Atkinson et al. (2006)
cis-butene	$1.1\times10^{-11}\times\exp(485/T)$	Atkinson et al. (2006)
trans-butene	$1.0\times10^{-11}\times\exp(553/T)$	Atkinson et al. (2006)
1,3-butadiene	$1.48\times10^{-11}\times\exp(448/T)$	Atkinson and Arey (2003)
Aromatics		
Benzene	$2.3\times10^{-12}\times\exp(-190/T)$	Atkinson et al. (2006)
Toluene	$1.8\times10^{-12}\times\exp(340/T)$	Atkinson et al. (2006)
Ethylbenzene	7×10^{-12}	Atkinson and Arey (2003)
Isopropylbenzene	6.3×10^{-12}	Atkinson and Arey (2003)
n-propylbenzene	5.8×10^{-12}	Atkinson and Arey (2003)
Styrene	5.8×10^{-11}	Atkinson and Arey (2003)
m+p-xylene	$1.87\times10^{-11,b}$	Atkinson and Arey (2003)
o-xylene	1.36×10^{-11}	Atkinson and Arey (2003)
1,3,5-trimethylbenzene	$1.32\times10^{-11}\times\exp(450/T)$	Bohn and Zetzsch (2012)
1,2,3-trimethylbenzene	$3.61\times10^{-12}\times\exp(620/T)$	Bohn and Zetzsch (2012)
1,2,4-trimethylbenzene	$2.73\times10^{-12}\times\exp(730/T)$	Bohn and Zetzsch (2012)
3-Ethyltoluene	1.2×10^{-11}	Atkinson and Arey (2003)
4-Ethyltoluene	1.2×10^{-11}	Atkinson and Arey (2003)
S/IVOCs		

S/IVOC	2×10^{-11}	Ma et al. (2017)
Biogenics		
Isoprene	2.7×10^{-11}×exp(390/T)	Atkinson et al. (2006)
α-pinene	1.2×10^{-11}×exp(440/T)	Atkinson et al. (2006)
β-pinene	1.55×10^{-11}×exp(467/T)	Atkinson and Arey (2003)
Radicals		
NO + RO_2	2.8×10^{-12}×exp(300/T)	Sander et al. (2011)
HO_2 + RO_2	4.1×10^{-13}×exp(750/T)	Sander et al. (2011)
RO_2 + RO_2	9.5×10^{-14}×exp(390/T)	Sander et al. (2011)

[a] Showing the rate constant at 298 K, 1013 hPa. However, for this study, we used the temperature and pressure dependent formulation listed in each respective reference.

[b] This is the average of m-xylene and p-xylene rate constants.

S6. Potential SOA Calculations

To determine the amount of SOA produced from the observed precursors, Eq. S3 was used, where *Y* is the stoichiometric aerosol yield for each hydrocarbon (RH) species *i*, similar to other studies (e.g., Zhao et al., 2014). The updated yields from Ma et al. (2017) were used, which incorporate a correction for the gas-phase partitioning of semi-volatile compounds to chamber walls (Krechmer et al., 2016). Since there were no direct measurements of S/IVOC concentrations, an estimated (Robinson et al., 2007; Dzepina et al., 2009) relationship between the amount of gas-phase S/IVOC co-emitted with POA at the typical temperatures (~20°C) and OA mass concentrations (~10 μg sm^{-3}) observed over Seoul were used. The POA is taken from Figure 5b and is within the range of values observed in other urban environments (Zhang et al., 2005; Hayes et al., 2013; Ait-Helal et al., 2014; Kim et al., 2018) (13 μg sm^{-3} ppmv^{-1} in Seoul versus 4.5 – 28.8 μg sm^{-3} ppmv^{-1} in other studies).

$$P(OA) = \sum_i Y_i \times \Delta RH_i \tag{S3}$$

$$\Delta RH = \frac{RH(t)}{e^{(-k[OH]t)}} - RH(t) \tag{S4}$$

The hydrocarbons measured on the DC-8 were the concentrations at time, *t*; thus, Eq. SS4 was used, which takes into account the amount of OH that oxidized the hydrocarbon (OH_{exp} =

[OH]*t*) between emissions and measurement, and *k* is the OH rate constant for each specific hydrocarbon (SI Table 3).

Finally, to determine the fate of the RO_2 radical in the reactions over Seoul (high/low NO_x regime), and thus, what aerosol yields to use, the RO_2 lifetime with reaction of NO, HO_2, and RO_2 versus photochemical age was calculated (Figure S22). The measured NO and HO_2 was used in the calculations, we assumed RO_2 was approximately the same concentration as HO_2 in this calculation (Thornton et al., 2002), and the rate constants in SI Table 3 were used to calculated the lifetime and fractional fate of RO_2. The fate of RO_2 with autoxidation is not included as the rate is still uncertain (Crounse et al., 2013) and it should be less important in highly polluted environments such as Seoul, especially at the lower photochemical ages (< 0.5 eq. days) where most SOA is observed to be formed. The dominant sink of RO_2 over Seoul during KORUS-AQ is the reaction with NO, suggesting that the SOA yields for “high NO” conditions should be used to describe the production of SOA.

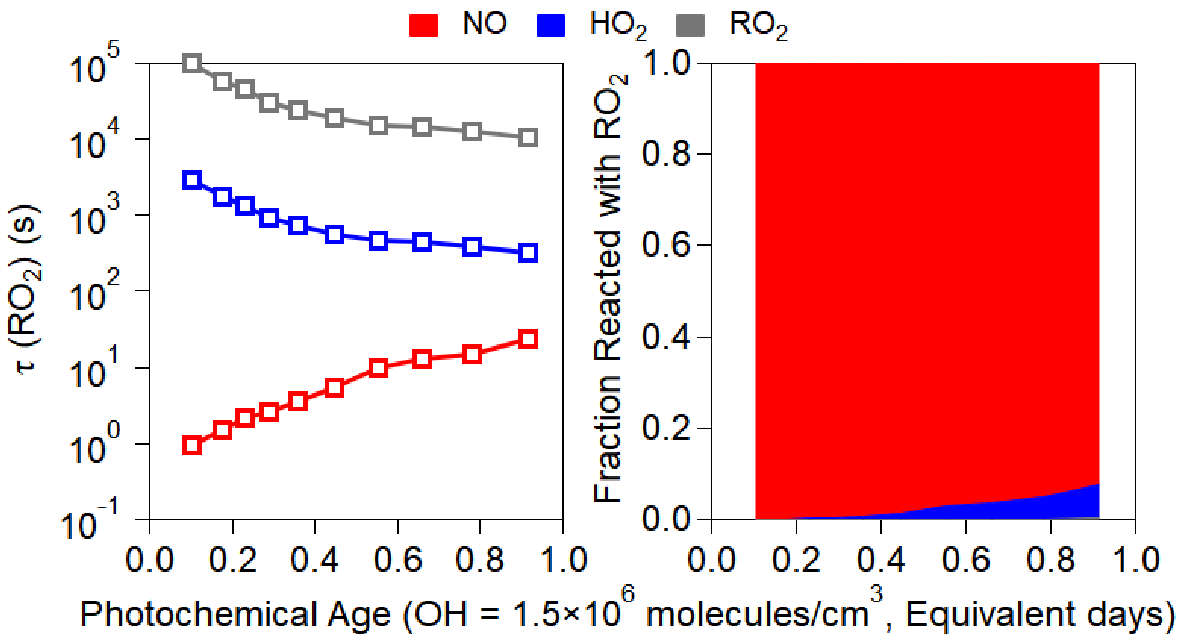

Figure S22. (left) Lifetime of RO_2 due to reactions with NO (red), HO_2 (blue), and RO_2 (grey) versus NO_x photochemical clock, normalized by OH = 1.5×10^{6} molecules/cm^{3}. (right) Fraction of RO_2 reacting with NO (red), HO_2 (blue), or RO_2 (red) versus NO_x photochemical clock, normalized by OH = 1.5×10^{6} molecules/cm^{3}. Values are calculated using observations over Seoul, South Korea, during KORUS-AQ, and RO_2 is assumed to be approximately equal to HO_2 (Thornton et al., 2002).

S7. FLEXPART Source Analysis

Source contributions have been estimated using Lagrangian backtrajectory calculations with the FLEXPART-WRF model (Brioude et al., 2013) in version 3.3.1, driven by meteorological output from NCEP GFS (NCEP) analyses downscaled to 5 km horizontal resolution using the Weather Research and Forecasting (WRF) model (Skamarock et al., 2008) in combination with the CREATE emission inventory (Woo et al., 2013). Approximately 20,000 parcels are released in 1 min intervals from the then-current location of the DC-8 during its research flights and parcel trajectories are followed back in time for 24 hours. The total time parcels spent in the lowermost 100 m—as surrogate for air having contact with an emission source at the ground—is recorded (residence time, [s kg^{-1} m^3]) and then folded with the emission fluxes ([kg m^{-2} s^{-1}]) given by the CREATE inventory for different compounds and source regions. This delivers an estimate of the source contribution (as increment in volume mixing ratio at the receptor, i.e., the DC-8 location) of the emissions of a given compound from a given region, assuming a perfect transport simulation and an inert compound.

S8. Intercomparisons of CU-AMS with Other Measurements on the NASA DC-8

We evaluate the measurement comparisons of the CU-AMS versus other aerosol measurements on-board the DC-8 during KORUS-AQ. We start with the mist chamber / ion chromatograph instrument (MC/IC), which has a comparable size cut as the AMS. The comparisons for SO_4 show good correlation ($R^2 = 0.76$) and slope close to 1 (0.95) (Figure S23). The higher scatter for the MC/IC is thought to arise from the lag and smearing in the measurements that has been observed in prior studies (TAbMET, 2009). For example, the correlation between instruments without lag and smearing have R^2 of 0.87 – 0.91 (CU-AMS versus extinction and CU-AMS vs K-AMS for certain RFs). If the MC/IC and CU-AMS SO_4 measurements are averaged to the sampling frequency of the University of New Hampshire filters (not shown), the R^2 improves (0.82) with no impact on the slope.

The comparison between the UNH filters and CU-AMS SO_4 shows higher R^2 (0.86) but lower slope (0.80), compared to MC/IC vs. CU-AMS. The higher R^2 is likely due to longer averaging time and lack of smearing that occurred with the MC/IC. As a comparison, the R^2 between MC/IC and filters are 0.84. The lower slope for the filters than the MC/IC is thought to be due to the different size cut-offs for the two measurements. For the filters, the upper size cut-off is ~4 μm (McNaughton et al., 2007); whereas, the upper size cut-off for the MC/IC is comparable to the AMS aerosol size cut-off (~ 1 μm aerodynamic). This means that the filter samples may include SO_4^{2-} from sea salt (sodium and calcium) and dust (calcium) (Heo et al., 2009; Kim et al., 2016; Heim et al., 2018). This is shown in Figure S24 and described in detail in Heim et al. (2018). Heim et al. (2018) found that dust dominated supermicron aerosol for approximately half of the campaign, and during these periods, supermicron SO_4^{2-} accounted for ~50% of the total SO_4^{2-} (sub plus supermicrong). Taken together, the comparisons of SO_4 mass concentrations from the CU-AMS from these two different methods (filter and MC/IC) indicate that the CU-AMS quantitatively captures the concentrations of SO_4.

Next, we compare the non-refractory species concentrations measured by the CU- and K-AMS. Intercomparisons between these two measurements for a few flights have been presented in prior publications (Hu et al., 2018a, 2018b). The K-AMS used a capture vaporizer, which leads to CE of ~1 for all ambient species (Hu et al., 2017a, 2017b; Xu et al., 2017). Here, we investigate the entire campaign. As shown in Figure S25, $R^2 > 0.80$ for all five species, and all slopes fall within ±20% of unity, which is within the combined uncertainty of both AMSs (~27%). However, at high concentrations (greater than ~5 – 10 μg sm^{-3}), the scatter between the two measurements increases, and for some species (e.g., SO_4), there is a slight curvature in the comparisons, where CU-AMS is greater than K-AMS. We believe this discrepancy originated from differences in transmission vs. particle size through the aerosol inlet and focusing lens (Figure S26). In-field calibrations showed that The K-AMS had 50% transmission at 615 nm (vacuum aerodynamic diameter; DeCarlo et al. (2004)), compared to the CU-AMS 50% transmission occurring at 900 nm. The reasons for the smaller transmission of the K-AMS are likely related to the PCI design (Bahreini et al., 2008, 2009) or possibly an underperforming aerodynamic lens in K-AMS (Liu et al., 2007). It was found that, in general, the RFs could be split between RFs generally below the K-AMS size cut-off (RFs 1 – 9, 11, 15, and 19) and above the size cut-off (RFs 10, 12 – 14, 16 – 18, 20) (Figure S27). The slopes and R^2 greatly improves for the observations below the K-AMS cut-off versus above (for slopes, 1.02 versus 0.84 and for R^2, 0.91 versus 0.82).

Finally, the ratios of the total AMS PM_1 masses measured by CU-AMS and K-AMS remain nearly constant about one (within ±11%) for the entire campaign and show no trend with estimated CE (for the standard vaporizer only) using the Middlebrook et al. (2012) algorithm (Figure S28).

Thus, when accounting for transmission effects, the two AMSs agree to within 10%, and the CU-AMS agrees to within 20% with the other co-located aerosol mass concentration measurements (filters and MC/IC) on the DC-8. This provides overall confidence in the calculated CE for the standard vaporizer (Middlebrook et al., 2012), RIE, and transmission of PM_1 for the CU-AMS measurements.

Besides directly comparing species mass, another well-established method to investigate aerosol instrument quantification is to compare the measured PM_1 mass (CU-AMS plus BC from SP2) versus the submicron extinction measured using methods described in Section 2.3.2 (nephlometer for scattering and absorption by PSAP) (e.g., DeCarlo et al., 2008). During KORUS-AQ, the slope between mass and extinction is 6.00 m^2 g^{-1} (Figure S29) with an R^2 of 0.87. The high correlation and similar slope compared to prior comparisons (Hand and Malm, 2007; DeCarlo et al., 2008; Dunlea et al., 2009; Shinozuka et al., 2009; Liu et al., 2017) indicates that the CU-AMS was not substantially impacted by the aerosol transmission effects discussed above. Also, the strong correlation ($R^2 = 0.87$) between the two instruments, which both have comparable, very high time resolution, indicate that the CU-AMS did not experience any plume recovery artifacts that were observed with the MC/IC or artifacts in measuring highly concentrated plumes.

Finally, we compare the PM_1 volume concentrations estimated from the LAS PM_1 versus the CU-AMS plus SP2. For this comparison, we use the calibrated AMS transmission curve during this campaign (Figure S30), which is consistent with those from recent studies (Knote et al., 2011; Hu et al., 2017b), to correct for particle transmission differences between the instruments. The LAS diameters were corrected by a factor of 1.115 from the PSL-calibrated values, to account for the lower refractive index of ambient particles, similar to Liu et al. (2017). To estimate the volume concentration from the combined AMS and BC measurements, we assume additive species volumes (DeCarlo et al., 2004). Species densities of 1.78 g cm^{-3} for NH_4, pNO_3, and SO_4 (Lide, 1991; Salcedo et al., 2006), 1.52 g cm^{-3} for Chl (Lide, 1991; Salcedo et al., 2006), 1.77 g cm^{-3} for BC (Park et al., 2004), and the OA density is estimated from the CU-AMS O/C and H/C ratios of OA using the parameterization of Kuwata et al. (2012). The comparison between total PM_1 volume estimated from the CU-AMS plus BC vs. versus LAS shows a correlation (R^2) of 0.86. However, the volume from AMS plus SP2 is higher (slope of 1.56) when comparing all of KORUS-AQ. We hypothesize that this may be due to saturation of the LAS detector at high particle concentrations that were frequently observed in this campaign (greater than 1800 particles cm^{-3} or total CU-AMS plus SP2 mass greater than 40 μg sm^{-3}), as has been observed in prior comparisons (Liu et al., 2017), or a change in the refractive index when OA becomes dominant at these high concentrations (Moise et al., 2015). Different filters are tested and shown in Figure S30 and Figure S***31***, using both values reported in literature and values that represent a stable ratio between LAS and calculated CU-AMS plus SP2 volume. If we filter for data when there is less than 20 μg sm^{-3}, the slope drops to 1.00, showing agreement between within the combined uncertainties ($R^2 = 0.79$), and providing strong evidence that LAS saturation at higher concentrations is the main reason for the apparent disagreement when analyzing the entire campaign.

We further investigate (Figure S31) whether the slope could be due to LAS saturation or a bias in RIE_{OA}, or in CE, vs. the values used in our analyses (Jimenez et al., 2016; Xu et al., 2018). There is a slight increase in the ratio of AMS plus SP2 to LAS volumes versus OA/total CU-AMS mass at high fractions of OA, although still within the combined measurement uncertainties. With filtered data (less than 1600 particles cm^{-3} or total CU-AMS mass less than 20 μg sm^{-3}), the volume ratios remain nearly flat, even at high *f*(OA). This confirms that LAS saturation is the most likely cause for the differences. Finally, a recent study (Xu et al., 2018) has reported new laboratory measurements of RIE_{OA} = 1.6±0.5, although these authors indicated that it was unclear whether this value was applicable to ambient particles, and the value of RIE_{OA} = 1.4 used in this study is well within their reported uncertainty. When using RIE_{OA} = 1.6 in our analysis (not shown) the slope for the entire dataset decrease by only 6% (1.56 to 1.47), indicating that RIE uncertainties cannot explain the bulk of the observed difference.

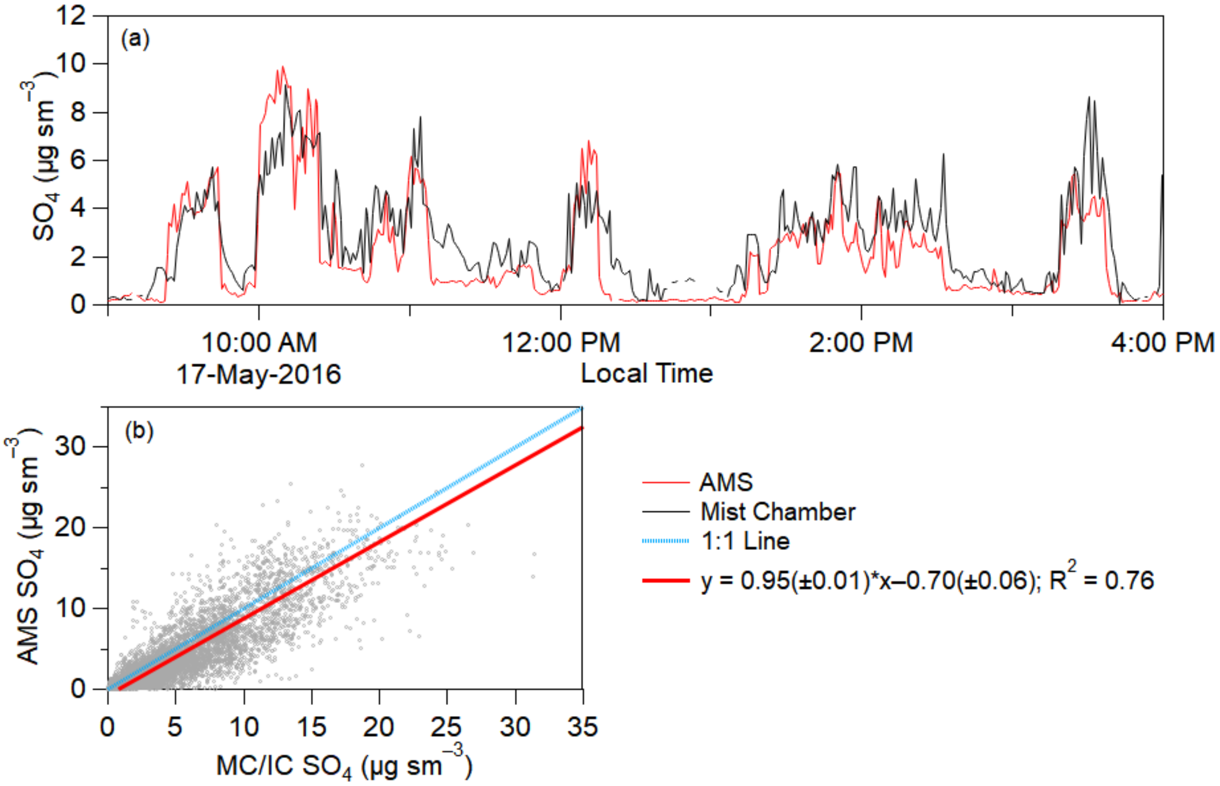

Figure S23. (top) Time series of mist-chamber (dark red line) and CU-AMS (red line) SO_4 for one flight (RF17). (bottom) Scatter plot of CU-AMS SO_4 versus mist-chamber ion-chromatograph (MC/IC) SO_4 for entire KORUS-AQ campaign.

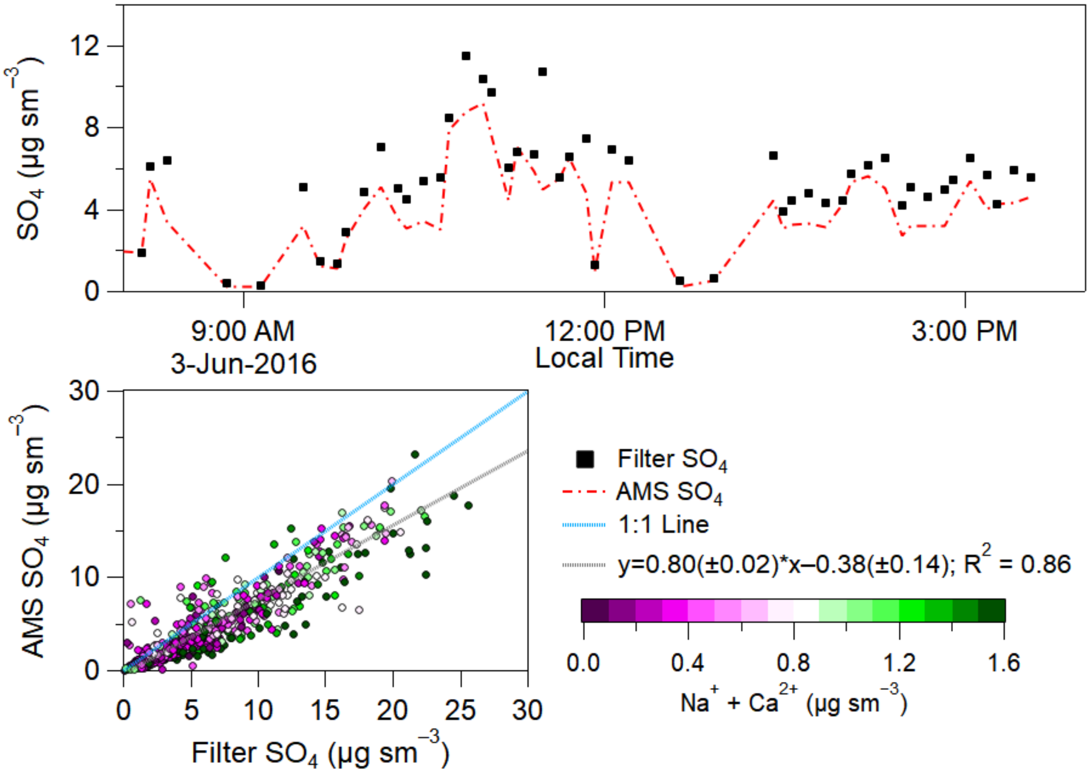

Figure S24. (top) Time series of filter (black squares) and CU-AMS (red line) SO_4 for one flight (RF17). The CU-AMS data has been averaged to the filter sampling time. (bottom) Scatter plot of CU-AMS SO_4 versus filter SO_4 for entire KORUS-AQ campaign. The points are colored by the total sodium (Na^+) and calcium (Ca^{2+}) measured by the filters, as indicators of sea salt and dust, respectively.

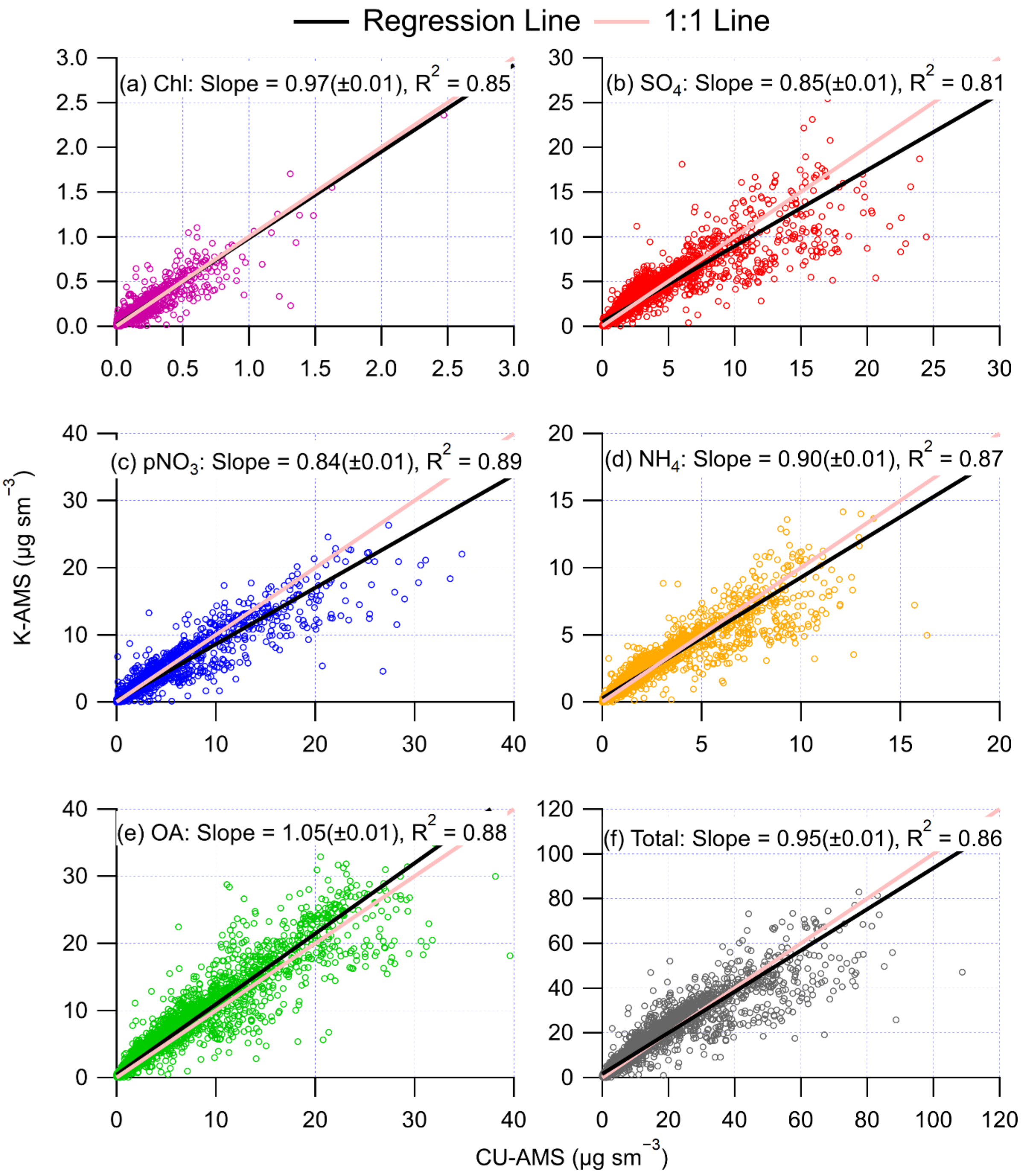

Figure S25. Scatter plot of not transmission corrected K-AMS versus CU-AMS mass concentrations for all of KORUS-AQ for (a) Chl, (b) SO_4, (c) pNO_3, (d) NH_4, (e) OA, and (f) total AMS mass. The slopes and R^2 for all comparisons are shown in each scatter plot.

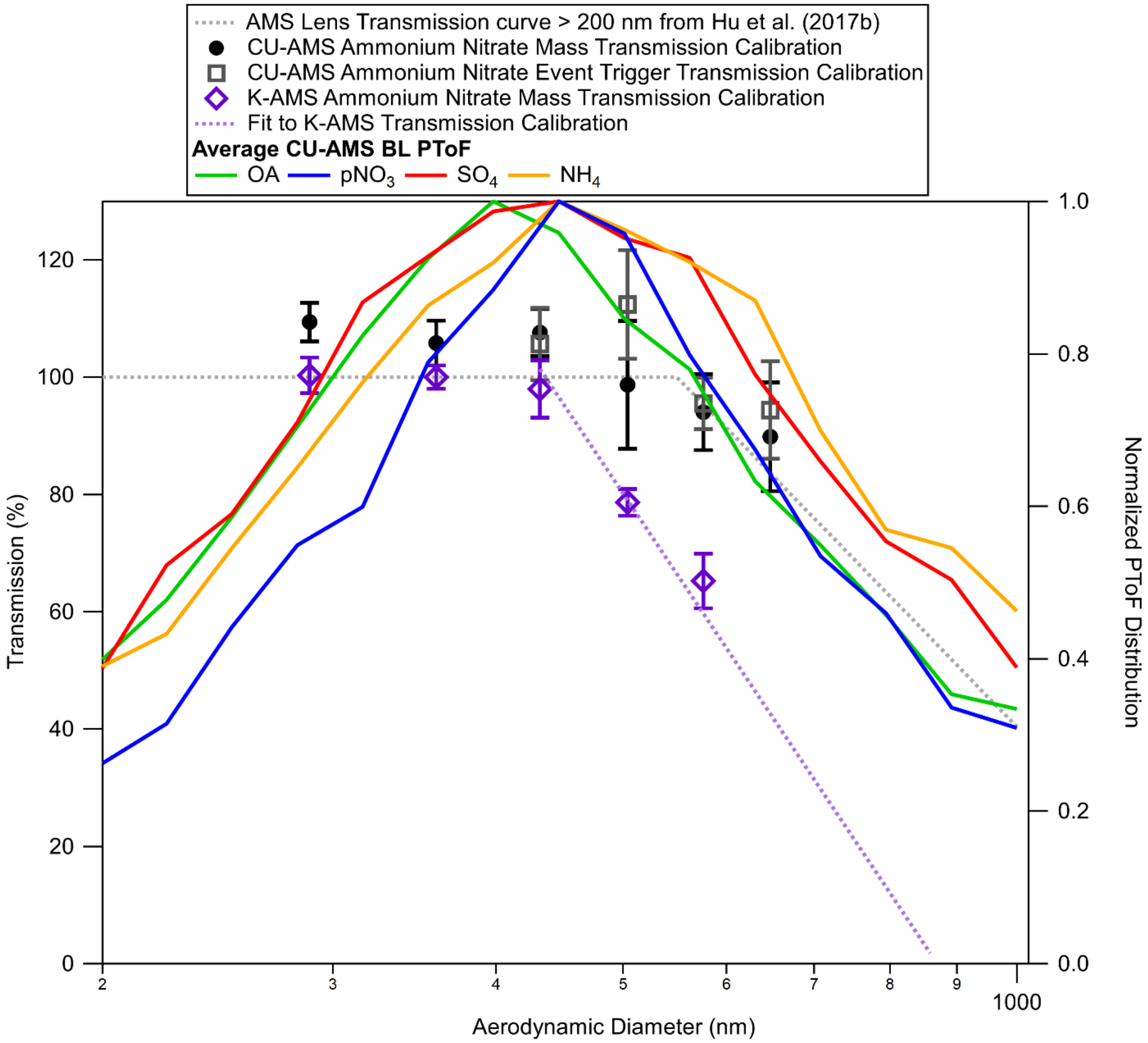

Figure S26. (left axis) Transmission curve for CU-AMS (black circle and dark grey square) and K-AMS (purple diamond). The curve from literature (Knote et al., 2011; Hu et al., 2017b), which describes the CU-AMS, is shown (grey dotted line). The fit for K-AMS transmission is shown with the purple dotted line. (right axis) Average mass distributions for OA (green), pNO_3 (blue), SO_4 (red), and NH_4 (orange) measured by CU-AMS in the boundary layer during KORUS-AQ. Note that some of the apparent signal at larger particle sizes is caused by the limited time response of the AMS detection system.

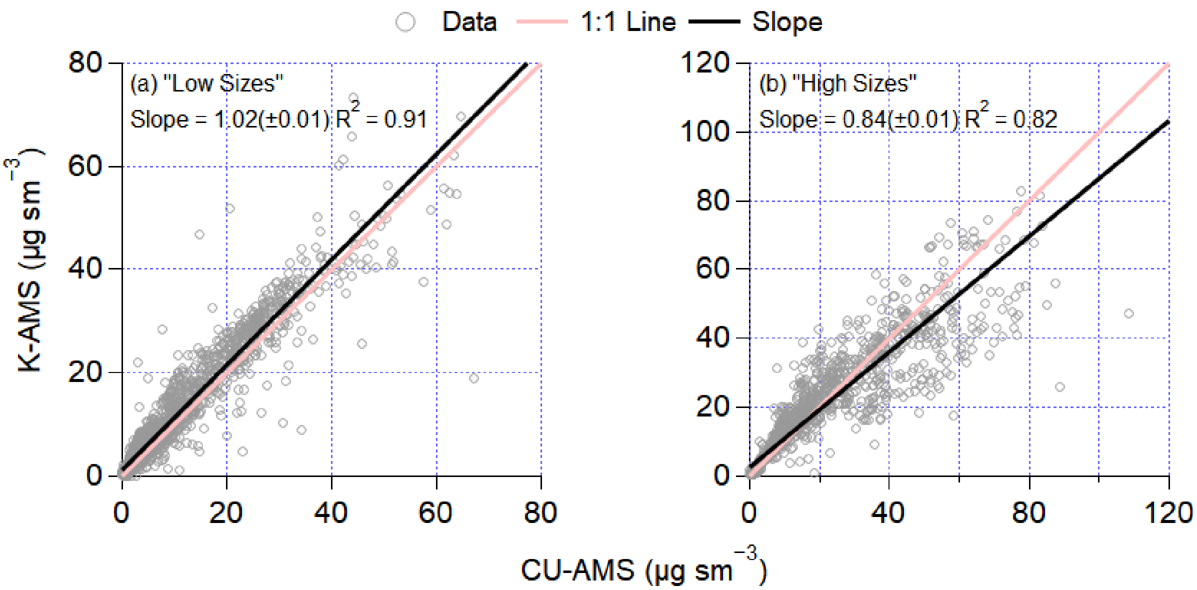

Figure S27. Scatter plot of K-AMS versus CU-AMS total mass concentrations (a) RFs 1 – 9, 11, 15, and 19 and (b) RFs 10, 12 – 14, 16 – 18, and 20. These are flights where the average sizes were found below (a) and above (b) the K-AMS size cut-off (Figure S26). The slopes and R^2 for all comparisons are shown in each scatter plot.

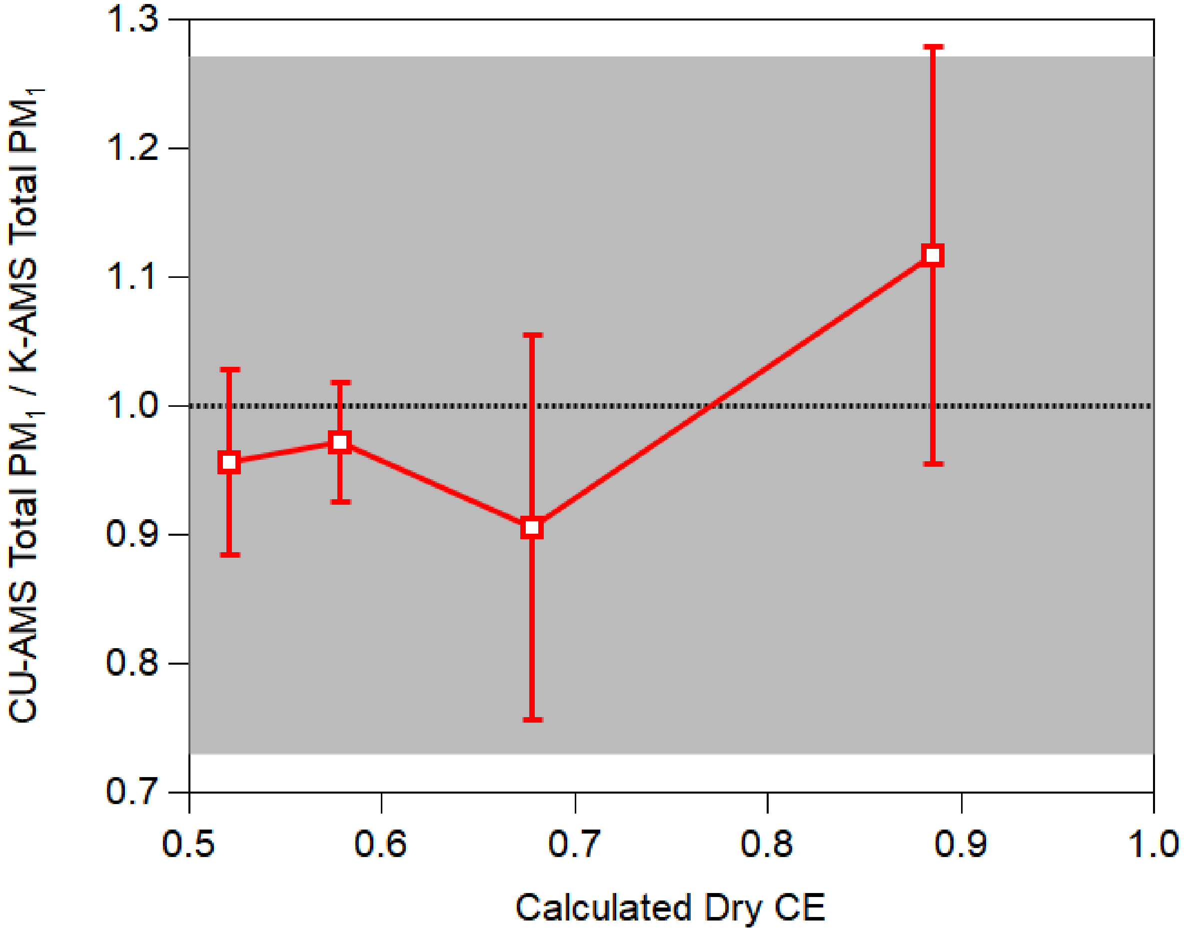

Figure S28. Binned total PM_1 AMS mass ratios, normalized by the average ratio, versus the calculated CE used for the CU-AMS measurements. The error bars are the standard error about the mean, and the shaded grey area is the combined uncertainty of the two AMS measurements (±27%). The data is only for flights where the PM_1 sizes were typically below the K-AMS size cut-off (RFs 1 – 9, 11, 15, and 19).

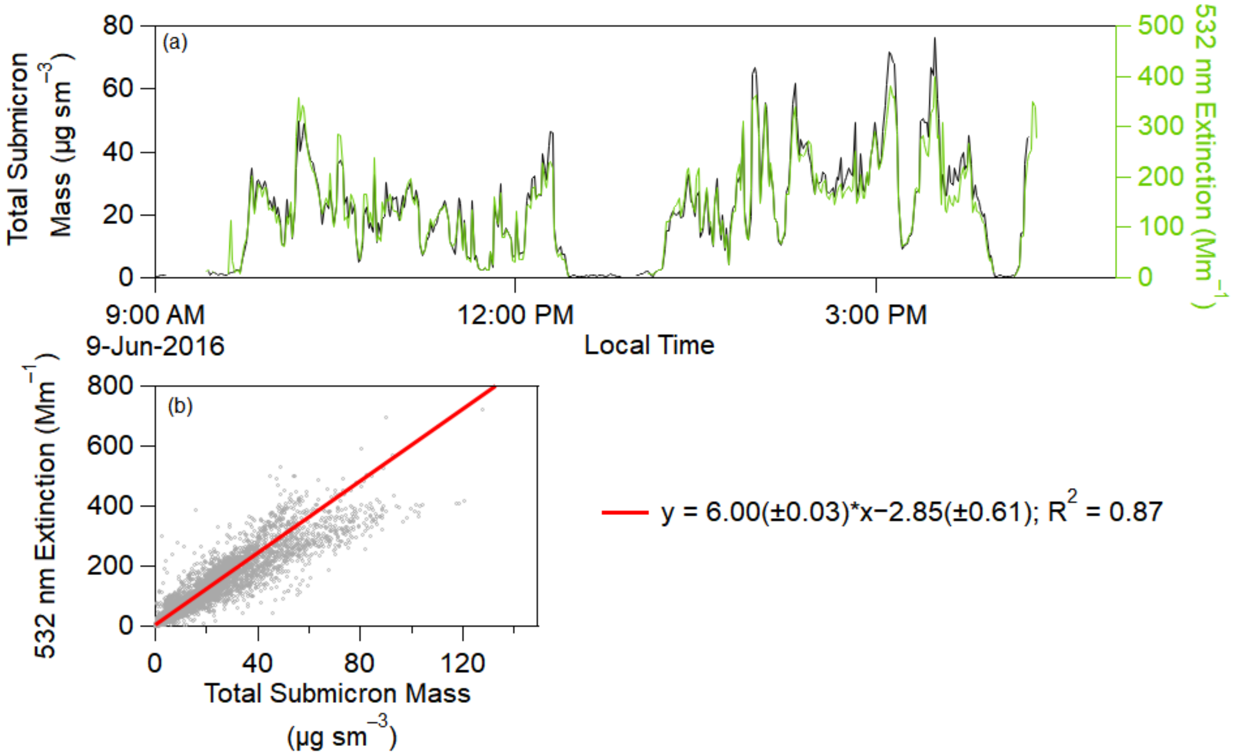

Figure S29. (top) Time series of total submicron mass (black, left axis) and 532 nm extinction (green, right axis) for one flight (RF19). (bottom) Scatter plot of 532 nm extinction versus total submicron mass (black carbon + CU-AMS species) for the entire KORUS-AQ campaign.

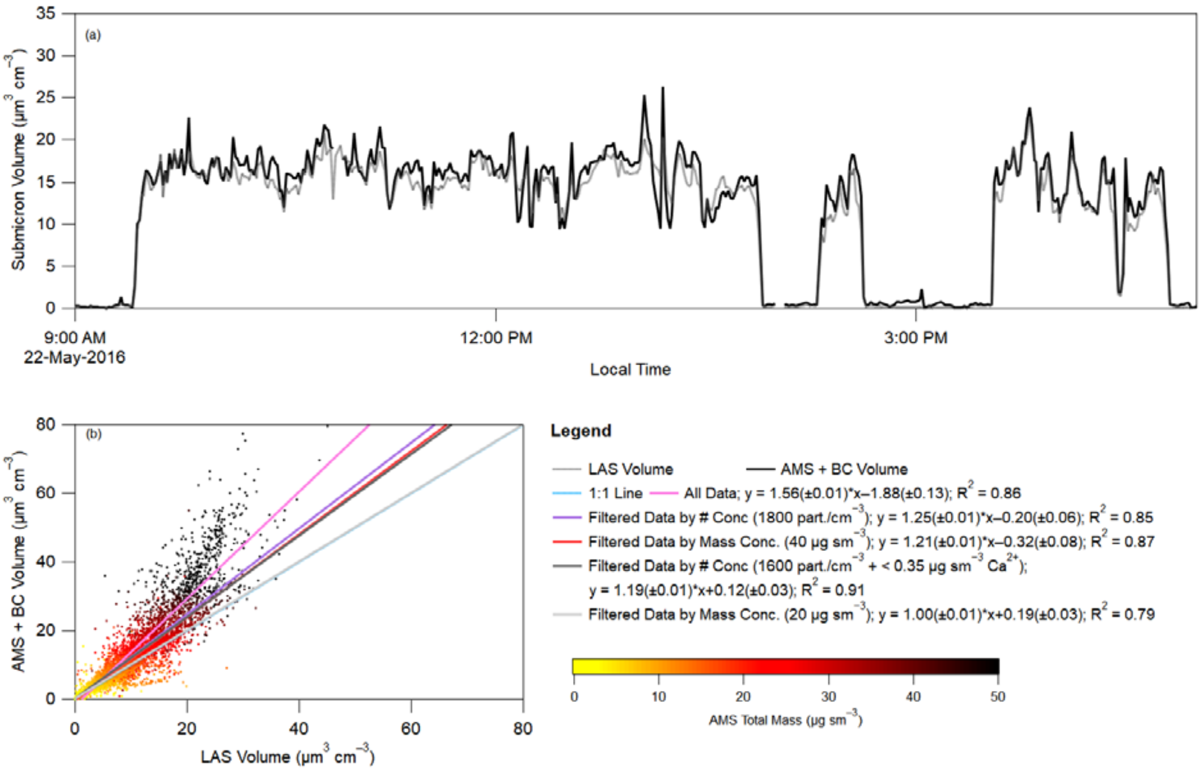

Figure S30. (top) Time series of total submicron volume from LAS (grey dashed line) and CU-AMS plus black carbon (black) for one flight (RF11). (bottom) Scatter plot of total submicron volume (black carbon + CU-AMS species) versus LAS volume for entire KORUS-AQ campaign. The data is colored by total CU-AMS mass. Pink line is a fit to all data, the purple line is a fit to data where the particle number concentration is less than 1800 particles scm^{-3}. The red line is a fit to the data where the CU-AMS plus SP2 total mass is less than 40 µg sm^{-3}. The black line is a fit to the data where the particle number concentration is less than 1600 particles scm^{-3} and Ca^{2+} concentration is less than 0.35 µg sm^{-3}. Finally, the grey line is a fit to the data where the CU-AMS plus BC total mass is less than 20 µg sm^{-3}.

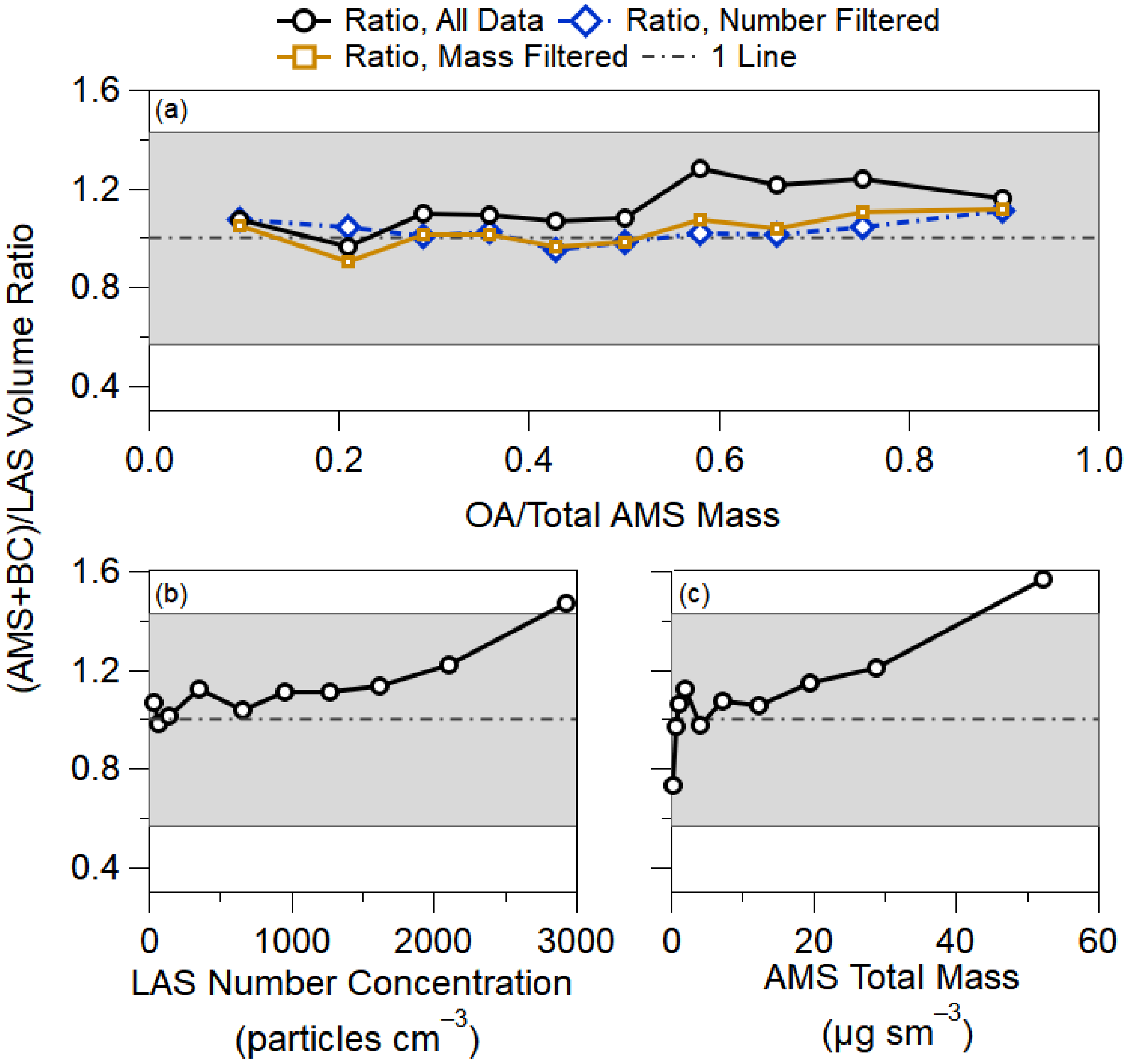

Figure S31. (a) Binned volume ratio (CU-AMS plus black carbon volume/LAS Volume) versus fraction of organic aerosol (OA) to total CU-AMS mass. (b) Binned volume ratio versus LAS particle number concentration. (c) Binned volume ratio versus CU-AMS total mass. In all figures, the black data is for all data whereas the blue data is for the volume ratio where the particle number concentration is less than 1600 particles cm^{-3} and the orange data is for the volume ratio where the CU-AMS total mass concentration is less than 20 µg sm^{-3}. Also, the shaded area represents the combined uncertainty in both measurements (Bahreini et al., 2009).

S9. Fractional PM_1 Contribution to Vertical Profile

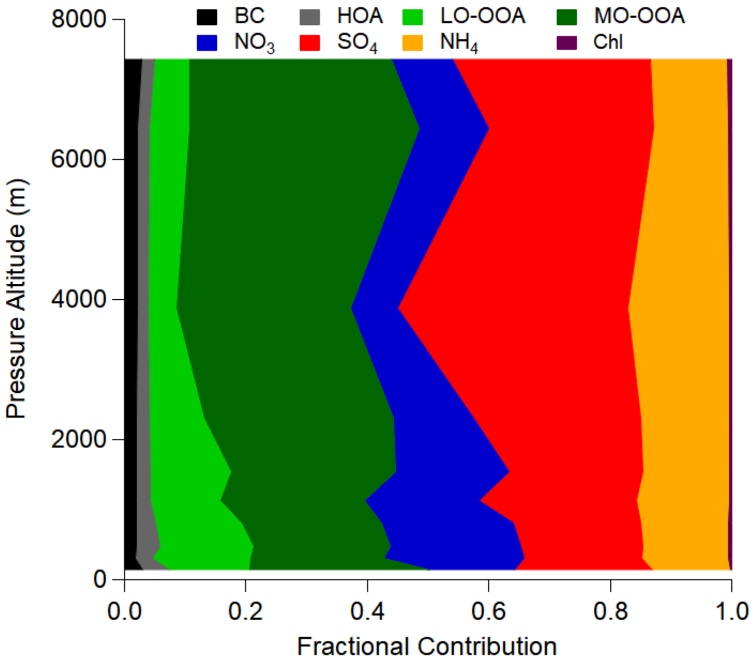

Figure S32. Fractional contribution of PM_1 contribution vertical profile for all of KORUS-AQ.

S10. Observed Aerosol Production over Seoul, South Korea

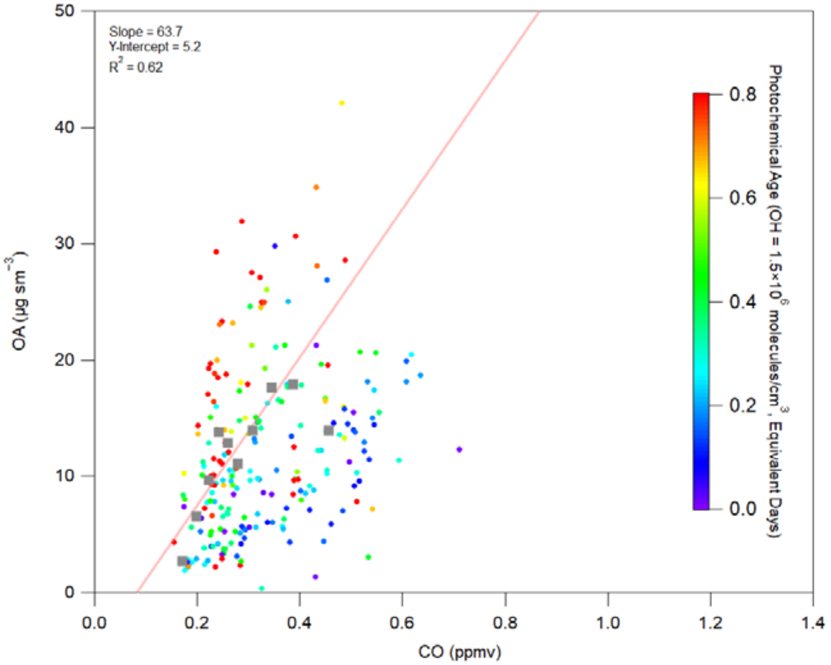

Figure S33. Scatter plot of OA versus CO, observed over Seoul, during KORUS-AQ. The points are colored by the NO_x photochemical clock. The fit is for the decile binned data.

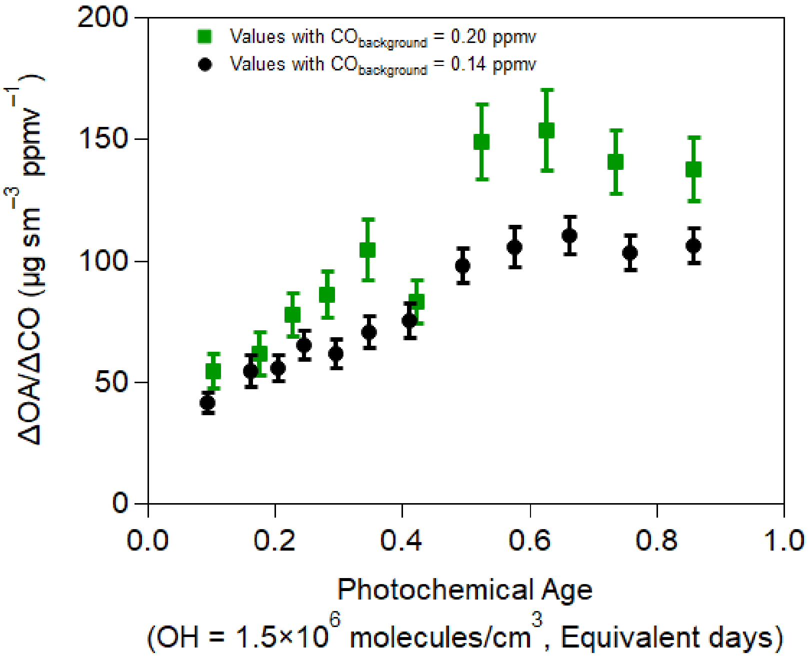

Figure S34. Comparison of ΔOA/ΔCO observed over Seoul with different CO backgrounds.

Table S4. Compilation of slopes used to convert from ΔOA/ΔCO to ΔOA/ΔCO₂ used in this study.

Location	*Slope (ppmv CO/ppmv CO_2)*	*Study*
Mexico City	0.045	Vay et al. (2009)
Los Angeles	0.009	Peischl et al., (2013)
Beijing	0.02	Wang et al. (2010) Silva et al. (2013) Tohjima et al. (2014)
Outflow China	0.02	Wang et al. (2010) Silva et al. (2013) Tohjima et al. (2014)
Seoul	0.01	Silva et al. (2013) Tang et al. (2018)

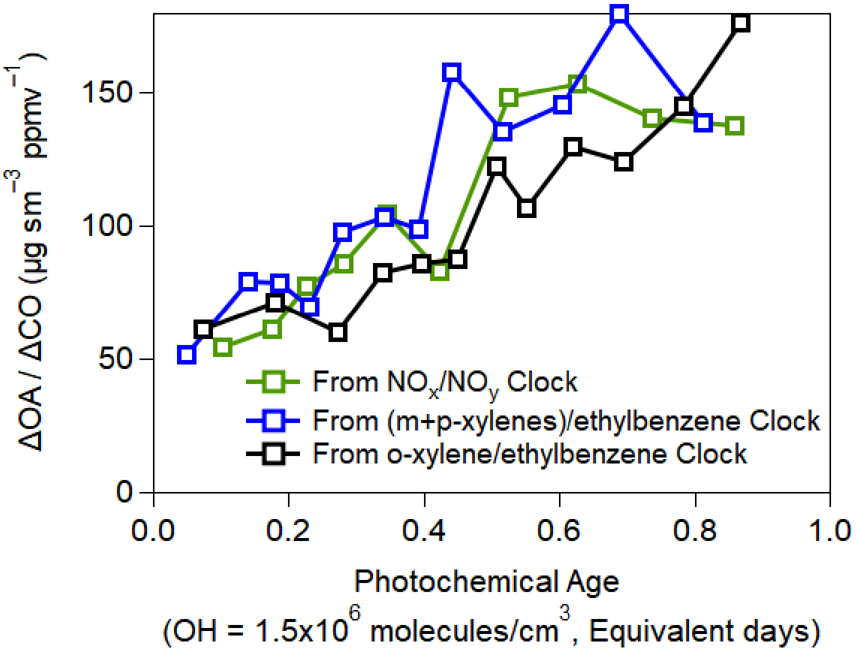

Figure S35. Same as **Figure 4**(a), but comparing results using three different photochemical clocks (Figure S21).

S11. Oxidation of OA

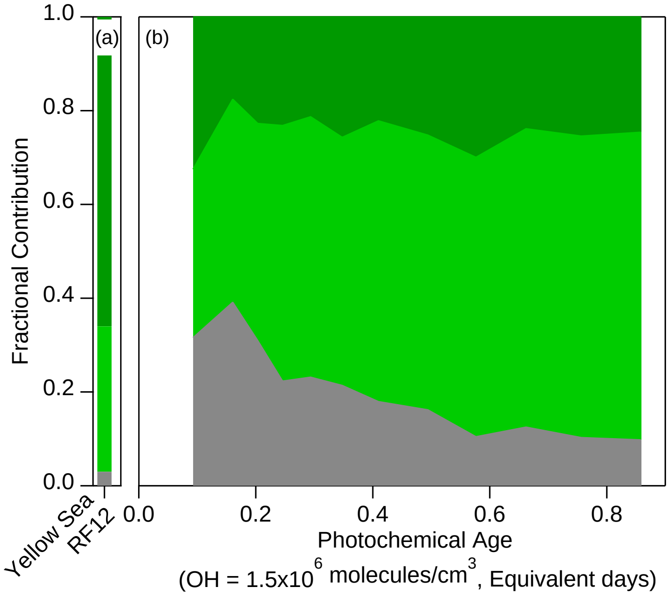

Figure S36. Same as **Figure 6**b, but speciated for MO-OOA, LO-OOA, and HOA. (a) is over the Yellow Sea (RF12) and (b) is over Seoul.

First, we briefly discuss how the AMS OA source tracers typically used to investigate OA chemistry evolved over Seoul (Figure S37). During KORUS-AQ, there was no appreciable influence from isoprene production of IEPOX-SOA (Hu et al., 2015), as the ion indicative of isoprene IEPOX-SOA ($C_5H_6O^+$) remained at background values typical of air without isoprene SOA influence.

Similarly, biomass burning OA (BBOA) appeared to be present but dilute in its contribution to OA. Most of the OA had $f_{C_2H_4O_2}$, an ion indicative of biomass burning and levoglucosan (Schneider et al., 2006; Aiken et al., 2010), below 0.1 over Seoul, and the PMF factors fall near the limit of detection for BBOA (Cubison et al., 2011) and lower than the values that typically indicate ambient and laboratory BBOA emissions at various stages of chemical evolution (Cubison et al., 2011; Ortega et al., 2013). We speculate that the limited BBOA is highly mixed into the OA from the numerous, small agricultural fires that were observed during the campaign and have been observed during this time period, during other years, in South Korea (Kang et al., 2006). However, the amount of fresher BBOA was not high enough, nor as strong of a feature as observed in prior studies (Aiken et al., 2010; DeCarlo et al., 2010; Cubison et al., 2011; Hu et al., 2016), to reliably resolve a separate BBOA PMF factor. As shown in Figure S11, typical gas-phase biomass burning tracers (CO, NO_x, acetonitrile, HCN, and black carbon) do not show a consistent strong correlation with any of the PMF factors, further suggesting that BBOA is not a major contributor, and any BBOA present is highly mixed with HOA and the oxidized OA. Consistent with our results, Kim et al. (2017) did not resolve a BBOA factor from a ground site in Seoul during the KORUS campaign.

Similar to other studies over urban areas or for chamber studies oxidizing urban VOCs (e.g., benzene, xylenes, etc.) (Ng et al., 2010; Freney et al., 2014; Ortega et al., 2016), marked chemical evolution was observed as tracked by the $C_2H_3O^+$ and CO_2^+ ions. The evolution of these two ions, as a fraction of total OA, fall in the same space as has been observed in these prior studies, indicating consistent photochemical evolution of SOA over urban locations.

Finally, unlike Kim et al. (2017), we did not observe clear indication for cooking organic aerosol (COA) in our PMF results. The COA was at a minimum (less than 1 $\mu g\ m^{-3}$) at the surface in Seoul during the times the DC-8 overpassed (Kim et al., 2018); thus, we speculate the amount of COA sampled was a small fraction of OA and was mostly lumped into the HOA factor. This does not affect our characterization of HOA as POA, since COA is also a primary aerosol emission.

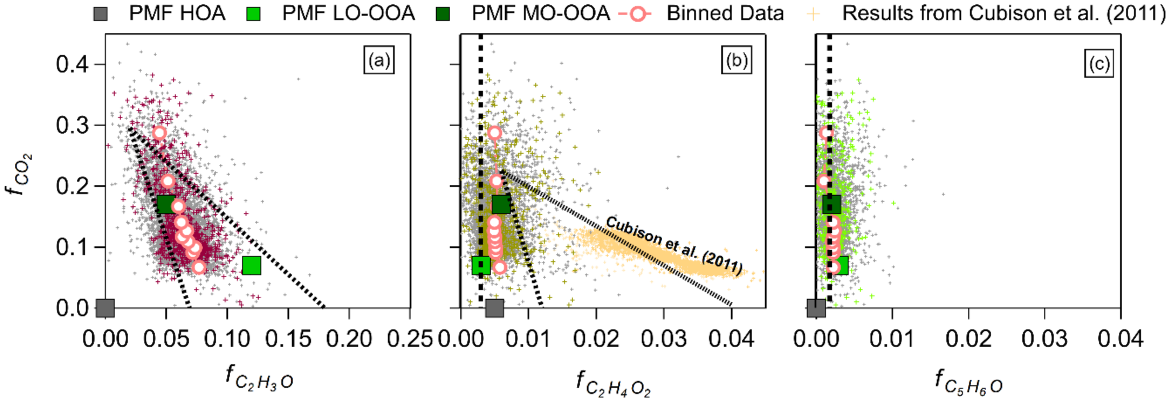

Figure S37. Plots of (a) f_{CO_2} versus $f_{C_2H_3O}$, (b) f_{CO_2} versus $f_{C_2H_4O_2}$, and (c) f_{CO_2} versus $f_{C_5H_6O}$. Points highlighted in color refer to observations over Seoul, South Korea, during KORUS-AQ. In (a), the triangle is from Ng et al. (2010); in (b), the triangle is from Cubison et al. (2011), and the vertical line is the typical "background" values for $f_{C_2H_4O_2}$ from Cubison et al. (2011); and, in (c), the vertical line is the typical "background" values for $f_{C_5H_6O}$ from Hu et al. (2015). The PMF results for each triangle plot are shown in squares, where grey is HOA, light green is LO-OOA, and dark green is MO-OOA. The light orange dots in (b) are the observations from ARCTAS forest fires (Cubison et al., 2011), as an example for data strongly impacted by biomass burning. The quantile average values (averaged the x variables according to quantiles of the y variables) for each comparison are shown in light red circles.

S12. Particle organic nitrates

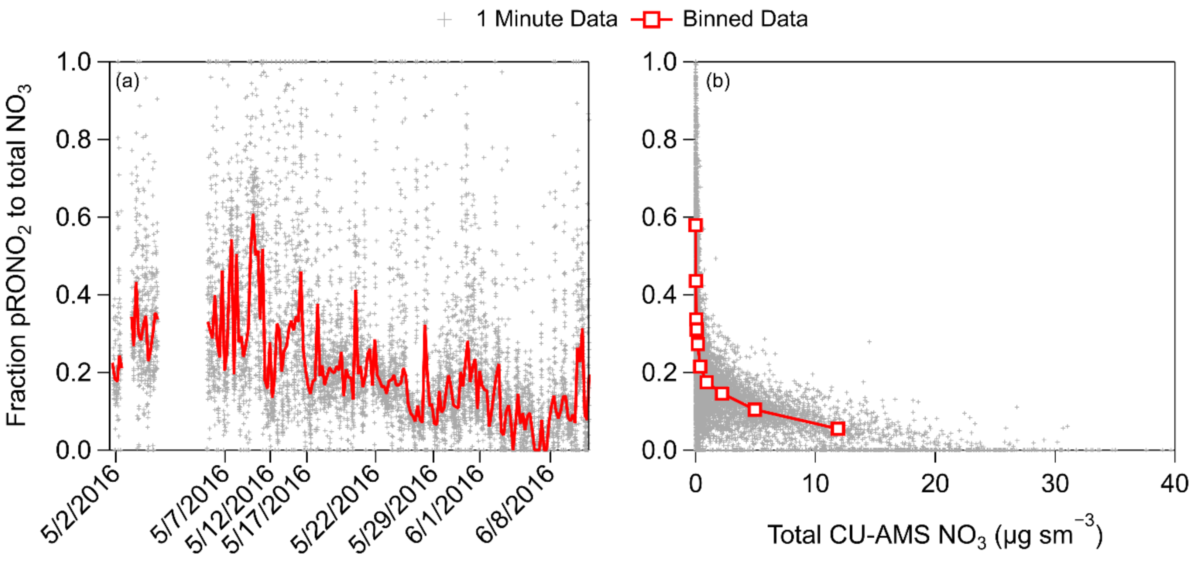

Figure S38. Time series of the fractional contribution of organic nitrates ($pRONO_2$) to the total pNO_3 signal during KORUS-AQ. (b) Fractional contribution of organic nitrates versus pNO_3 during KORUS-AQ.

References

Aiken, A. C., de Foy, B., Wiedinmyer, C., DeCarlo, P. F., Ulbrich, I. M., Wehrli, M. N., Szidat, S., Prévôt, A. S. H., Noda, J., Wacker, L., Volkamer, R., Fortner, E., Wang, J., Laskin, A., Shutthanandan, V., Zheng, J., Zhang, R., Paredes-Miranda, G., Arnott, W. P., Molina, L. T., Sosa, G., Querol, X. and Jimenez, J. L.: Mexico City aerosol analysis during MILAGRO using high resolution aerosol mass spectrometry at the urban supersite (T0)-Part 2: Analysis of the biomass burning contribution and the non-fossil carbon fraction, Atmos. Chem. Phys., 10(12), 5315–5341, doi:10.5194/acp-10-5315-2010, 2010.

Ait-Helal, W., Borbon, A., Sauvage, S., De Gouw, J. A., Colomb, A., Gros, V., Freutel, F., Crippa, M., Afif, C., Baltensperger, U., Beekmann, M., Doussin, J.-F. F., Durand-Jolibois, R., Fronval, I., Grand, N., Leonardis, T., Lopez, M., Michoud, V., Miet, K., Perrier, S., Prévôt, A. S. H., Schneider, J., Siour, G., Zapf, P. and Locoge, N.: Volatile and intermediate volatility organic compounds in suburban Paris: Variability, origin and importance for SOA formation, Atmos. Chem. Phys., 14(19), 10439–10464, doi:10.5194/acp-14-10439-2014, 2014.

Aknan, A. and Chen, G.: KORUS-AQ DC-8 Aircraft Dataset, [online] Available from: https://www-air.larc.nasa.gov/cgi-bin/ArcView/korusaq (Accessed 6 December 2018), 2018.

Atkinson, R.: Kinetics of the gas-phase reactions of OH radicals with alkanes and cycloalkanes, Atmos. Chem. Phys., 3(6), 2233–2307, doi:10.5194/acp-3-2233-2003, 2003.

Atkinson, R. and Arey, J.: Atmospheric Degradation of Volatile Organic Compounds, Chem. Rev., 103, 4605–4638, doi:10.1021/CR0206420, 2003.

Atkinson, R., Baulch, D. L., Cox, R. A., Crowley, J. N., Hampson, R. F., Hynes, R. G., Jenkin, M. E., Rossi, M. J. and Troe, J.: Evaluated kinetic and photochemical data for atmospheric chemistry: Volume I - gas phase reactions of Ox, HO_x , NO_x and SO_x species, Atmos. Chem. Phys., 4(6), 1461–1738, doi:10.5194/acp-4-1461-2004, 2004.

Atkinson, R., Baulch, D. L., Cox, R. A., Crowley, J. N., Hampson, R. F., Hynes, R. G., Jenkin, M. E., Rossi, M. J., Troe, J. and IUPAC Subcommittee: Evaluated kinetic and photochemical data for atmospheric chemistry: Volume II - gas phase reactions of organic species, Atmos. Chem. Phys., 6(11), 3625–4055, doi:10.5194/acp-6-3625-2006, 2006.

Bahreini, R., Dunlea, E. J., Matthew, B. M., Simons, C., Docherty, K. S., DeCarlo, P. F., Jimenez, J. L., Brock, C. A. and Middlebrook, A. M.: Design and Operation of a Pressure-Controlled Inlet for Airborne Sampling with an Aerodynamic Aerosol Lens, Aerosol Sci. Technol., 42(6), 465–471, doi:10.1080/02786820802178514, 2008.

Bahreini, R., Ervens, B., Middlebrook, A. M., Warneke, C., de Gouw, J. A., DeCarlo, P. F., Jimenez, J. L., Brock, C. A., Neuman, J. A., Ryerson, T. B., Stark, H., Atlas, E., Brioude, J., Fried, A., Holloway, J. S., Peischl, J., Richter, D., Walega, J., Weibring, P., Wollny, A. G. and Fehsenfeid, F. C.: Organic aerosol formation in urban and industrial plumes near Houston and Dallas, Texas, J. Geophys. Res., 114(16), D00F16, doi:10.1029/2008JD011493, 2009.

Bohn, B. and Zetzsch, C.: Kinetics and mechanism of the reaction of OH with the trimethylbenzenes – experimental evidence for the formation of adduct isomers, Phys. Chem. Chem. Phys., 14(40), 13933, doi:10.1039/c2cp42434g, 2012.

Brioude, J., Arnold, D., Stohl, A., Cassiani, M., Morton, D., Seibert, P., Angevine, W., Evan, S., Dingwell, A., Fast, J. D., Easter, R. C., Pisso, I., Burkhart, J. and Wotawa, G.: The Lagrangian particle dispersion model FLEXPART-WRF version 3.1, Geosci. Model Dev., 6(6), 1889–1904, doi:10.5194/gmd-6-1889-2013, 2013.

Crounse, J. D., Nielsen, L. B., Jørgensen, S., Kjaergaard, H. G. and Wennberg, P. O.: Autoxidation of Organic Compounds in the Atmosphere, J. Phys. Chem. Lett., 4(20), 3513–3520, doi:10.1021/jz4019207, 2013.

Cubison, M. J., Ortega, A. M., Hayes, P. L., Farmer, D. K., Day, D. A., Lechner, M. J., Brune, W. H., Apel, E., Diskin, G. S., Fisher, J. A., Fuelberg, H. E., Hecobian, A., Knapp, D. J., Mikoviny, T., Riemer, D., Sachse, G. W., Sessions, W., Weber, R. J., Weinheimer, A. J., Wisthaler, A. and Jimenez, J. L.: Effects of aging on organic aerosol from open biomass burning smoke in aircraft and laboratory studies, Atmos. Chem. Phys., 11(23), 12049–12064, doi:10.5194/acp-11-12049-2011, 2011.

de Gouw, J. A., Gilman, J. B., Kim, S.-W., Lerner, B. M., Isaacman-VanWertz, G., McDonald, B. C., Warneke, C., Kuster, W. C., Lefer, B. L., Griffith, S. M., Dusanter, S., Stevens, P. S. and Stutz, J.: Chemistry of Volatile Organic Compounds in the Los Angeles basin: Nighttime Removal of Alkenes and Determination of Emission Ratios, J. Geophys. Res., 122(21), 11,843-11,861, doi:10.1002/2017JD027459, 2017.

DeCarlo, P. F., Slowik, J. G., Worsnop, D. R., Davidovits, P., Jimenez, J. L., Stainken, K., Williams, L., Jayne, J., Kolb, C. and Rudich, Y.: Particle Morphology and Density Characterization by Combined Mobility and Aerodynamic Diameter Measurements. Part 1: Theory, Aerosol Sci. Technol., 38(12), 1185–1205, doi:10.1080/027868290903907, 2004.

DeCarlo, P. F., Dunlea, E. J., Kimmel, J. R., Aiken, A. C., Sueper, D., Crounse, J., Wennberg, P. O., Emmons, L., Shinozuka, Y., Clarke, A., Zhou, J., Tomlinson, J., Collins, D. R., Knapp, D., Weinheimer, A. J., Montzka, D. D., Campos, T. and Jimenez, J. L.: Fast airborne aerosol size and chemistry measurements above Mexico City and Central Mexico during the MILAGRO campaign, Atmos. Chem. Phys., 8(14), 4027–4048, doi:10.5194/acp-8-4027-2008, 2008.

DeCarlo, P. F., Ulbrich, I. M., Crounse, J., de Foy, B., Dunlea, E. J., Aiken, A. C., Knapp, D., Weinheimer, A. J., Campos, T., Wennberg, P. O. and Jimenez, J. L.: Investigation of the sources and processing of organic aerosol over the Central Mexican Plateau from aircraft measurements during MILAGRO, Atmos. Chem. Phys., 10(12), 5257–5280, doi:10.5194/acp-10-5257-2010, 2010.

Docherty, K. S., Aiken, A. C., Huffman, J. A., Ulbrich, I. M., DeCarlo, P. F., Sueper, D., Worsnop, D. R., Snyder, D. C., Peltier, R. E., Weber, R. J., Grover, B. D., Eatough, D. J., Williams, B. J., Goldstein, A. H., Ziemann, P. J. and Jimenez, J. L.: The 2005 Study of Organic Aerosols at Riverside (SOAR-1): instrumental intercomparisons and fine particle composition, Atmos. Chem. Phys., 11(23), 12387–12420, doi:DOI 10.5194/acp-11-12387-2011, 2011.

Dunlea, E. J., DeCarlo, P. F., Aiken, A. C., Kimmel, J. R., Peltier, R. E., Weber, R. J., Tomlison, J., Collins, D. R., Shinozuka, Y., McNaugthon, C. S., Howell, S. G., Clarke, A. D., Emmons, L. K., Apel, E. C., Pfister, G. G., van Donkelaar, A., Martin, R. V., Millett, D. B., Heald, C. L. and Jimenez, J. L.: Evolution of Asian aerosols during transpacific transport in INTEX-B, Atmos. Chem. Phys., 9(19), 7257–7287, doi:10.5194/acp-9-7257-2009, 2009.

Dzepina, K., Volkamer, R. M. R., Madronich, S., Tulet, P., Ulbrich, I. M., Zhang, Q., Cappa, C. D., Ziemann, P. J. and Jimenez, J. L.: Evaluation of recently-proposed secondary organic aerosol models for a case study in Mexico City, Atmos. Chem. Phys., 9(15), 5681–5709, doi:10.5194/acp-9-5681-2009, 2009.

Freney, E. J., Sellegri, K., Canonaco, F., Colomb, A., Borbon, A., Michoud, V., Doussin, J.-F., Crumeyrolle, S., Amarouche, N., Pichon, J.-M., Bourianne, T., Gomes, L., Prevot, A. S. H., Beekmann, M. and Schwarzenböeck, A.: Characterizing the impact of urban emissions on regional aerosol particles: airborne measurements during the MEGAPOLI experiment, Atmos. Chem. Phys., 14(3), 1397–1412, doi:10.5194/acp-14-1397-2014, 2014.

Fry, J. L., Draper, D. C., Zarzana, K. J., Campuzano-Jost, P., Day, D. A., Jimenez, J. L., Brown, S. S., Cohen, R. C., Kaser, L., Hansel, A., Cappellin, L., Karl, T., Hodzic Roux, A., Turnipseed, A., Cantrell, C., Lefer, B. L. and Grossberg, N.: Observations of gas- and aerosol-phase organic nitrates at BEACHON-RoMBAS 2011, Atmos. Chem. Phys., 13(17), 8585–8605, doi:10.5194/acp-13-8585-2013, 2013.

Hand, J. L. and Malm, W. C.: Review of aerosol mass scattering efficiencies from ground-based measurements since 1990, J. Geophys. Res., 112(D16), D16203, doi:10.1029/2007JD008484, 2007.

Hayes, P. L., Ortega, A. M., Cubison, M. J., Froyd, K. D., Zhao, Y., Cliff, S. S., Hu, W. W., Toohey, D. W., Flynn, J. H., Lefer, B. L., Grossberg, N., Alvarez, S., Rappenglück, B., Taylor, J. W., Allan, J. D., Holloway, J. S., Gilman, J. B., Kuster, W. C., de Gouw, J. A., Massoli, P., Zhang, X., Liu, J., Weber, R. J., Corrigan, A. L., Russell, L. M., Isaacman, G., Worton, D. R., Kreisberg, N. M., Goldstein, A. H., Thalman, R., Waxman, E. M., Volkamer, R., Lin, Y. H., Surratt, J. D., Kleindienst, T. E., Offenberg, J. H., Dusanter, S., Griffith, S., Stevens, P. S., Brioude, J., Angevine, W. M. and Jimenez, J. L.: Organic aerosol composition and sources in Pasadena, California, during the 2010 CalNex campaign, J. Geophys. Res., 118(16), 9233–9257, doi:10.1002/jgrd.50530, 2013.

Heim, E., Dibb, J., Scheuer, E., Campuzano-Jost, P., Nault, B. A., Jimenez, J. L., Peterson, D., Knote, C., Fenn, M., Hair, J., Beyersdorf, A. J. and Anderson, B. E.: Asian Dust Observed during KORUS-AQ Facilitates the Uptake and Incorporation of Soluble Pollutants during Transport to South Korea: The Hwangsa Anthropogenic Model, J. Geophys. Res. Atmos., submitted, 2018.

Heo, J.-B., Hopke, P. K. and Yi, S.-M.: Source apportionment of PM2.5 in Seoul, Korea, Atmos. Chem. Phys., 9(14), 4957–4971, doi:10.5194/acp-9-4957-2009, 2009.

Hu, W., Hu, M., Hu, W., Jimenez, J. L., Yuan, B., Chen, W., Wang, M., Wu, Y., Chen, C., Wang, Z., Peng, J., Zeng, L. and Shao, M.: Chemical composition, sources and aging process of sub-micron aerosols in Beijing: contrast between summer and winter, J. Geophys. Res. Atmos., doi:10.1002/2015JD024020, 2016.

Hu, W., Campuzano-Jost, P., Day, D. A., Croteau, P., Canagaratna, M. R., Jayne, J. T., Worsnop, D. R. and Jimenez, J. L.: Evaluation of the new capture vaporizer for aerosol mass spectrometers (AMS) through field studies of inorganic species, Aerosol Sci. Technol., 51(6), 735–754, doi:10.1080/02786826.2017.1296104, 2017a.

Hu, W., Campuzano-Jost, P., Day, D. A., Croteau, P., Canagaratna, M. R., Jayne, J. T., Worsnop, D. R. and Jimenez, J. L.: Evaluation of the new capture vapourizer for aerosol mass spectrometers (AMS) through laboratory studies of inorganic species, Atmos. Meas. Tech., 10(6), 2897–2921, doi:10.5194/amt-10-2897-2017, 2017b.

Hu, W., Day, D. A., Campuzano-Jost, P., Nault, B. A., Park, T., Lee, T., Croteau, P., Canagaratna,

M. R., Jayne, J. T., Worsnop, D. R. and Jimenez, J. L.: Evaluation of the new capture vaporizer for Aerosol Mass Spectrometers: Characterization of organic aerosol mass spectra, Aerosol Sci. Technol., 52(7), 752–739, doi:10.1080/02786826.2018.1454584, 2018a.

Hu, W., Day, D. A., Campuzano-Jost, P., Nault, B. A., Park, T., Lee, T., Croteau, P., Canagaratna, M. R., Jayne, J. T., Worsnop, D. R. and Jimenez, J. L.: Evaluation of the New Capture Vaporizer for Aerosol Mass Spectrometers (AMS): Elemental Composition and Source Apportionment of Organic Aerosols (OA), ACS Earth Sp. Chem., 2(4), 410–421, doi:10.1021/acsearthspacechem.8b00002, 2018b.

Hu, W. W., Campuzano-Jost, P., Palm, B. B., Day, D. A., Ortega, A. M., Hayes, P. L., Krechmer, J. E., Chen, Q., Kuwata, M., Liu, Y. J., de Sá, S. S., McKinney, K., Martin, S. T., Hu, M., Budisulistiorini, S. H., Riva, M., Surratt, J. D., St. Clair, J. M., Isaacman-Van Wertz, G., Yee, L. D., Goldstein, A. H., Carbone, S., Brito, J., Artaxo, P., de Gouw, J. A., Koss, A., Wisthaler, A., Mikoviny, T., Karl, T., Kaser, L., Jud, W., Hansel, A., Docherty, K. S., Alexander, M. L., Robinson, N. H., Coe, H., Allan, J. D., Canagaratna, M. R., Paulot, F. and Jimenez, J. L.: Characterization of a real-time tracer for Isoprene Epoxydiols-derived Secondary Organic Aerosol (IEPOX-SOA) from aerosol mass spectrometer measurements, Atmos. Chem. Phys., 15(8), 11807–11833, doi:10.5194/acp-15-11807-2015, 2015.

Huffman, J. A., Docherty, K. S., Aiken, A. C., Cubison, M. J., Ulbrich, I. M., DeCarlo, P. F., Sueper, D., Jayne, J. T., Worsnop, D. R., Ziemann, P. J. and Jimenez, J. L.: Chemically-resolved aerosol volatility measurements from two megacity field studies, Atmos. Chem. Phys., 9(1), 7161–7182, doi:doi:10.5194/acp-9-7161-2009, 2009.

Jimenez, J. L., Canagaratna, M. R., Donahue, N. M., Prevot, A. S. H., Zhang, Q., Kroll, J. H., DeCarlo, P. F., Allan, J. D., Coe, H., Ng, N. L., Aiken, A. C., Docherty, K. S., Ulbrich, I. M., Grieshop, A. P., Robinson, A. L., Duplissy, J., Smith, J. D., Wilson, K. R., Lanz, V. A., Hueglin, C., Sun, Y. L., Tian, J., Laaksonen, A., Raatikainen, T., Rautiainen, J., Vaattovaara, P., Ehn, M., Kulmala, M., Tomlinson, J. M., Collins, D. R., Cubison, M. J., Dunlea, E. J., Huffman, J. A., Onasch, T. B., Alfarra, M. R., Williams, P. I., Bower, K., Kondo, Y., Schneider, J., Drewnick, F., Borrmann, S., Weimer, S., Demerjian, K., Salcedo, D., Cottrell, L., Griffin, R., Takami, A., Miyoshi, T., Hatakeyama, S., Shimono, A., Sun, J. Y., Zhang, Y. M., Dzepina, K., Kimmel, J. R., Sueper, D., Jayne, J. T., Herndon, S. C., Trimborn, A. M., Williams, L. R., Wood, E. C., Middlebrook, A. M., Kolb, C. E., Baltensperger, U., Worsnop, D. R. and Worsnop, D. R.: Evolution of organic aerosols in the atmosphere., Science, 326(5959), 1525–1529, doi:10.1126/science.1180353, 2009.

Jimenez, J. L., Canagaratna, M. R., Drewnick, F., Allan, J. D., Alfarra, M. R., Middlebrook, A. M., Slowik, J. G., Zhang, Q., Coe, H., Jayne, J. T. and Worsnop, D. R.: Comment on "The effects of molecular weight and thermal decomposition on the sensitivity of a thermal desorption aerosol mass spectrometer," Aerosol Sci. Technol., 50(9), i–xv, doi:10.1080/02786826.2016.1205728, 2016.

Kang, C. M., Kang, B. W. and Lee, H. S.: Source identification and trends in concentrations of gaseous and fine particulate principal species in Seoul, South Korea, J. Air Waste Manag. Assoc., 56(7), 911–921, doi:10.1080/10473289.2006.10464506, 2006.

Kim, B. M., Seo, J., Kim, J. Y., Lee, J. Y. and Kim, Y.: Transported vs. local contributions from secondary and biomass burning sources to PM2.5, Atmos. Environ., 144, 24–36, doi:10.1016/j.atmosenv.2016.08.072, 2016.

Kim, H., Zhang, Q. and Heo, J.: Influence of Intense secondary aerosol formation and long-range transport on aerosol chemistry and properties in the Seoul Metropolitan Area during spring time : Results from KORUS-AQ, Atmos. Chem. Phys., 18, 7149–7168, doi:10.51944/acp-2017-947, 2018.

Kleinman, L. I., Springston, S. R., Daum, P. H., Lee, Y.-N., Nunnermacker, L. J., Senum, G. I., Wang, J., Weinstein-Lloyd, J., Alexander, M. L., Hubbe, J., Ortega, J., Canagaratna, M. R. and Jayne, J.: The time evolution of aerosol composition over the Mexico City plateau, Atmos. Chem. Phys., 8(6), 1559–1575, doi:10.5194/acp-8-1559-2008, 2008.

Knote, C., Brunner, D., Vogel, H., Allan, J., Asmi, A., Äijälä, M., Carbone, S., van der Gon, H. D., Jimenez, J. L., Kiendler-Scharr, A., Mohr, C., Poulain, L., Prévôt, A. S. H., Swietlicki, E. and Vogel, B.: Towards an online-coupled chemistry-climate model: evaluation of trace gases and aerosols in COSMO-ART, Geosci. Model Dev., 4(4), 1077–1102, doi:10.5194/gmd-4-1077-2011, 2011.

Krechmer, J. E., Pagonis, D., Ziemann, P. J. and Jimenez, J. L.: Quantification of Gas-Wall Partitioning in Teflon Environmental Chambers Using Rapid Bursts of Low-Volatility Oxidized Species Generated in Situ, Environ. Sci. Technol., 50(11), 5757–5765, doi:10.1021/acs.est.6b00606, 2016.

Kuwata, M., Zorn, S. R. and Martin, S. T.: Using Elemental Ratios to Predict the Density of Organic Material Composed of Carbon, Hydrogen, and Oxygen, Environ. Sci. Technol., 46(2), 787–794, doi:10.1021/es202525q, 2012.

Lide, D. R.: CRC Handbook of Chemistry and Physics, CRC Press Inc., USA., 1991.

Liu, P. S. K., Deng, R., Smith, K. A., Williams, L. R., Jayne, J. T., Canagaratna, M. R., Moore, K., Onasch, T. B., Worsnop, D. R. and Deshler, T.: Transmission Efficiency of an Aerodynamic Focusing Lens System: Comparison of Model Calculations and Laboratory Measurements for the Aerodyne Aerosol Mass Spectrometer, Aerosol Sci. Technol., 41(8), 721–733, doi:10.1080/02786820701422278, 2007.

Liu, X., Huey, L. G., Yokelson, R. J., Selimovic, V., Simpson, I. J., Müller, M., Jimenez, J. L., Campuzano-Jost, P., Beyersdorf, A. J., Blake, D. R., Butterfield, Z., Choi, Y., Crounse, J. D., Day, D. A., Diskin, G. S., Dubey, M. K., Fortner, E., Hanisco, T. F., Hu, W., King, L. E., Kleinman, L., Meinardi, S., Mikoviny, T., Onasch, T. B., Palm, B. B., Peischl, J., Pollack, I. B., Ryerson, T. B., Sachse, G. W., Sedlacek, A. J., Shilling, J. E., Springston, S., St. Clair, J. M., Tanner, D. J., Teng, A. P., Wennberg, P. O., Wisthaler, A. and Wolfe, G. M.: Airborne measurements of western U.S. wildfire emissions: Comparison with prescribed burning and air quality implications, J. Geophys. Res., 122(11), 6108–6129, doi:10.1002/2016JD026315, 2017.

Ma, P. K., Zhao, Y., Robinson, A. L., Worton, D. R., Goldstein, A. H., Ortega, A. M., Jimenez, J.-L., Zotter, P., Prévôt, A. S. H., Szidat, S. and Hayes, P. L.: Evaluating the impact of new observational constraints on P-S/IVOC emissions, multi-generation oxidation, and chamber wall losses on SOA modeling for Los Angeles, CA, Atmos. Chem. Phys., 17(15), 9237–9259, doi:10.5194/acp-17-9237-2017, 2017.

McNaughton, C. S., Clarke, A. D., Howell, S. G., Pinkerton, M., Anderson, B., Thornhill, L., Hudgins, C., Winstead, E., Dibb, J. E., Scheuer, E. and Maring, H.: Results from the DC-8 Inlet

Characterization Experiment (DICE): Airborne versus surface sampling of mineral dust and sea salt aerosols, Aerosol Sci. Technol., 41(2), 136–159, doi:10.1080/02786820601118406, 2007.

Middlebrook, A. M., Bahreini, R., Jimenez, J. L. and Canagaratna, M. R.: Evaluation of Composition-Dependent Collection Efficiencies for the Aerodyne Aerosol Mass Spectrometer using Field Data, Aerosol Sci. Technol., 46(3), 258–271, doi:10.1080/02786826.2011.620041, 2012.

Moise, T., Flores, J. M. and Rudich, Y.: Optical Properties of Secondary Organic Aerosols and Their Changes by Chemical Processes, Chem. Rev., 115(10), 4400–4439, doi:10.1021/cr5005259, 2015.

Mollner, A. K., Valluvadasan, S., Feng, L., Sprague, M. K., Okumura, M., Milligan, D. B., Bloss, W. J., Sander, S. P., Martien, P. T., Harley, R. a, McCoy, A. B. and Carter, W. P. L.: Rate of Gas Phase Association of Hydroxyl Radical and Nitrogen Dioxide, Science (80-.)., 330(6004), 646–9, doi:10.1126/science.1193030, 2010.

Murphy, D. M.: The effects of molecular weight and thermal decomposition on the sensitivity of a thermal desorption aerosol mass spectrometer, Aerosol Sci. Technol., 50(2), 118–125, doi:10.1080/02786826.2015.1136403, 2016.

Nault, B. A., Campuzano-Jost, P., Schroder, J. C., Sueper, D. and Jimenez, J. L.: Using Event Trigger Panel for IE/AB and Transmission Curve Calibrations, in 17th AMS Users' Meeting, Portland. [online] Available from: http://cires1.colorado.edu/jimenez-group/wiki/index.php/AMSUsrMtgs#17th_AMS_Users_Meeting.2C_Portland.2C_Oregon, 2016.

NCEP: National Centers for Environmental Prediction, [online] Available from: http://www.emc.ncep.noaa.gov/GFS/doc.php (Accessed 16 November 2017), n.d.

Neuman, J. A., Parrish, D. D., Ryerson, T. B., Brock, C. A., Wiedinmyer, C., Frost, G. J., Holloway, J. S. and Fehsenfeld, F. C.: Nitric acid loss rates measured in power plant plumes, J. Geophys. Res., 109(23), 1–13, doi:10.1029/2004JD005092, 2004.

Ng, N. L., Canagaratna, M. R., Zhang, Q., Jimenez, J. L., Tian, J., Ulbrich, I. M., Kroll, J. H., Docherty, K. S., Chhabra, P. S., Bahreini, R., Murphy, S. M., Seinfeld, J. H., Hildebrandt, L., Donahue, N. M., Decarlo, P. F., Lanz, V. A., Prévôt, A. S. H., Dinar, E., Rudich, Y. and Worsnop, D. R.: Organic aerosol components observed in Northern Hemispheric datasets from Aerosol Mass Spectrometry, Atmos. Chem. Phys., 10(10), 4625–4641, doi:10.5194/acp-10-4625-2010, 2010.

Nguyen, T. B., Crounse, J. D., Teng, A. P., St. Clair, J. M., Paulot, F., Wolfe, G. M. and Wennberg, P. O.: Rapid deposition of oxidized biogenic compounds to a temperate forest, Proc. Natl. Acad. Sci., 112(5), E392–E401, doi:10.1073/pnas.1418702112, 2015.

Ortega, A. M., Day, D. A., Cubison, M. J., Brune, W. H., Bon, D., de Gouw, J. A. and Jimenez, J. L.: Secondary organic aerosol formation and primary organic aerosol oxidation from biomass-burning smoke in a flow reactor during FLAME-3, Atmos. Chem. Phys., 13(22), 11551–11571, doi:10.5194/acp-13-11551-2013, 2013.

Ortega, A. M., Hayes, P. L., Peng, Z., Palm, B. B., Hu, W., Day, D. A., Li, R., Cubison, M. J., Brune, W. H., Graus, M., Warneke, C., Gilman, J. B., Kuster, W. C., de Gouw, J. A., Gutiérrez-Montes, C. and Jimenez, J. L.: Real-time measurements of secondary organic aerosol formation and aging from ambient air in an oxidation flow reactor in the Los Angeles area, Atmos. Chem.

Phys., 16(11), 7411–7433, doi:10.5194/acp-16-7411-2016, 2016.

Palm, B. B., Campuzano-Jost, P., Ortega, A. M., Day, D. A., Kaser, L., Jud, W., Karl, T., Hansel, A., Hunter, J. F., Cross, E. S., Kroll, J. H., Peng, Z., Brune, W. H. and Jimenez, J. L.: In situ secondary organic aerosol formation from ambient pine forest air using an oxidation flow reactor, Atmos. Chem. Phys., 16(5), 2943–2970, doi:10.5194/acp-16-2943-2016, 2016.

Palm, B. B., Campuzano-Jost, P., Day, D. A., Ortega, A. M., Fry, J. L., Brown, S. S., Zarzana, K. J., Dube, W., Wagner, N. L., Draper, D. C., Kaser, L., Jud, W., Karl, T., Hansel, A., Gutiérrez-Montes, C. and Jimenez, J. L.: Secondary organic aerosol formation from in situ OH, O3, and NO3 oxidation of ambient forest air in an oxidation flow reactor, Atmos. Chem. Phys., 17(8), 5331–5354, doi:10.5194/acp-17-5331-2017, 2017.

Palm, B. B., de Sá, S. S., Day, D. A., Campuzano-Jost, P., Hu, W., Seco, R., Sjostedt, S. J., Park, J.-H., Guenther, A. B., Kim, S., Brito, J., Wurm, F., Artaxo, P., Thalman, R., Wang, J., Yee, L. D., Wernis, R., Isaacman-VanWertz, G., Goldstein, A. H., Liu, Y., Springston, S. R., Souza, R., Newburn, M. K., Alexander, M. L., Martin, S. T. and Jimenez, J. L.: Secondary organic aerosol formation from ambient air in an oxidation flow reactor in central Amazonia, Atmos. Chem. Phys., 18(1), 467–493, doi:10.5194/acp-18-467-2018, 2018.

Park, K., Kittelson, D. B., Zachariah, M. R. and McMurry, P. H.: Measurement of Inherent Material Density of Nanoparticle Agglomerates, J. Nanoparticle Res., 6(2/3), 267–272, doi:10.1023/B:NANO.0000034657.71309.e6, 2004.

Parrish, D. D., Stohl, A., Forster, C., Atlas, E. L., Blake, D. R., Goldan, P. D., Kuster, W. C. and de Gouw, J. A.: Effects of mixing on evolution of hydrocarbon ratios in the troposphere, J. Geophys. Res., 112(D10), D10S34, doi:10.1029/2006JD007583, 2007.

Peischl, J., Ryerson, T. B., Brioude, J., Aikin, K. C., Andrews, A. E., Atlas, E., Blake, D., Daube, B. C., de Gouw, J. A., Dlugokencky, E., Frost, G. J., Gentner, D. R., Gilman, J. B., Goldstein, A. H., Harley, R. A., Holloway, J. S., Kofler, J., Kuster, W. C., Lang, P. M., Novelli, P. C., Santoni, G. W., Trainer, M., Wofsy, S. C. and Parrish, D. D.: Quantifying sources of methane using light alkanes in the Los Angeles basin, California, J. Geophys. Res. Atmos., 118(10), 4974–4990, doi:10.1002/jgrd.50413, 2013.

Peng, Z., Day, D. A., Stark, H., Li, R., Lee-Taylor, J., Palm, B. B., Brune, W. H. and Jimenez, J. L.: HO_x radical chemistry in oxidation flow reactors with low-pressure mercury lamps systematically examined by modeling, Atmos. Meas. Tech., 8(11), 4863–4890, doi:10.5194/amt-8-4863-2015, 2015.

Pieber, S. M., El Haddad, I., Slowik, J. G., Canagaratna, M. R., Jayne, J. T., Platt, S. M., Bozzetti, C., Daellenbach, K. R., Fröhlich, R., Vlachou, A., Klein, F., Dommen, J., Miljevic, B., Jiménez, J. L., Worsnop, D. R., Baltensperger, U. and Prévôt, A. S. H.: Inorganic Salt Interference on CO2+ in Aerodyne AMS and ACSM Organic Aerosol Composition Studies, Environ. Sci. Technol., 50(19), 10494–10503, doi:10.1021/acs.est.6b01035, 2016.

Robinson, A. L., Donahue, N. M., Shrivastava, M. K., Weitkamp, E. A., Sage, A. M., Grieshop, A. P., Lane, T. E., Pierce, J. R. and Pandis, S. N.: Rethinking Organic Aerosols: Semivolatile Emissions and Photochemical Aging, Science (80-.)., 315(5816), 1259–1262, doi:10.1126/science.1133061, 2007.

Romer, P. S., Duffey, K. C., Wooldridge, P. J., Allen, H. M., Ayres, B. R., Brown, S. S., Brune,

W. H., Crounse, J. D., de Gouw, J., Draper, D. C., Feiner, P. A., Fry, J. L., Goldstein, A. H., Koss, A., Misztal, P. K., Nguyen, T. B., Olson, K., Teng, A. P., Wennberg, P. O., Wild, R. J., Zhang, L. and Cohen, R. C.: The lifetime of nitrogen oxides in an isoprene-dominated forest, Atmos. Chem. Phys., 16(12), 7623–7637, doi:10.5194/acp-16-7623-2016, 2016.

Salcedo, D., Onasch, T. B., Dzepina, K., Canagaratna, M. R., Zhang, Q., Huffman, J. A., Decarlo, P. F., Jayne, J. T., Mortimer, P., Worsnop, D. R., Kolb, C. E., Johnson, K. S., Zuberi, B., Marr, L. C., Volkamer, R., Molina, L. T., Molina, M. J., Cardenas, B., Bernabe, R. M., Marquez, C., Gaffney, J. S., Marley, N. A., Laskin, A., Shutthanandan, V., Xie, Y., Brune, W., Lesher, R., Shirley, T. and Jimenez, J. L.: Characterization of ambient aerosols in Mexico City during the MCMA-2003 campaign with Aerosol Mass Spectrometry: results from the CENICA Supersite, Atmos. Chem. Phys., 6(4), 925–946, doi:10.5194/acp-6-925-2006, 2006.

Sander, S. P., Abbatt, J. P. D., Barker, J. R., Burkholder, J. B., Friedl, R. R., Golden, D. M., Huie, R. E., Kolb, C. E., Kurylo, M. J., Moortgat, G. K., Orkin, V. L. and Wine, P. H.: Chemical Kinetics and Photochemical Data for Use in Atmospheric Studies, Evaluation No. 17, JPL Publ. 10-6, Jet Propuls. Lab. Pasadena, 2011.

Schneider, J., Hings, S. S., Nele Hock, B., Weimer, S., Borrmann, S., Fiebig, M., Petzold, A., Busen, R. and Kärcher, B.: Aircraft-based operation of an aerosol mass spectrometer: Measurements of tropospheric aerosol composition, J. Aerosol Sci., 37(7), 839–857, doi:10.1016/j.jaerosci.2005.07.002, 2006.

Shinozuka, Y., Clarke, A. D., DeCarlo, P. F., Jimenez, J. L., Dunlea, E. J., Roberts, G. C., Tomlinson, J. M., Collins, D. R., Howell, S. G., Kapustin, V. N., McNaughton, C. S. and Zhou, J.: Aerosol optical properties relevant to regional remote sensing of CCN activity and links to their organic mass fraction: airborne observations over Central Mexico and the US West Coast during MILAGRO/INTEX-B, Atmos. Chem. Phys., 9(18), 6727–6742, 2009.

Silva, S. J., Arellano, A. F. and Worden, H. M.: Toward anthropogenic combustion emission constraints from space-based analysis of urban CO_2/CO sensitivity, Geophys. Res. Lett., 40(18), 4971–4976, doi:10.1002/grl.50954, 2013.

Skamarock, C., Klemp, B., Dudhia, J., Gill, O., Barker, D., Duda, G., Huang, X., Wang, W. and Powers, G.: A Description of the Advanced Research WRF Version 3, , doi:10.5065/D68S4MVH, 2008.

Sprengnether, M. M., Demerjian, K. L., Dransfield, T. J., Clarke, J. S., Anderson, J. G. and Donahue, N. M.: Rate Constants of Nine C6-C9 Alkanes with OH from 230 to 379 K: Chemical Tracers for [OH], J. Phys. Chem. A2, 113, 5030–5038, doi:10.1021/jp810412m, 2009.

TAbMET: TAbMEP Assessment: POLARCAT HNO3 Summary, in TAbMEP POLARCAT/ICARTT Analysis, edited by G. Chen, https://www-air.larc.nasa.gov/TAbMEP2_polarcat.html, Boulder., 2009.

Tang, W., Arellano, A. F., DiGangi, J. P., Choi, Y., Diskin, G. S., Agustí-Panareda, A., Parrington, M., Massart, S., Gaubert, B., Lee, Y., Kim, D., Jung, J., Hong, J., Hong, J.-W., Kanaya, Y., Lee, M., Stauffer, R. M., Thompson, A. M., Flynn, J. H. and Woo, J.-H.: Evaluating High-Resolution Forecasts of Atmospheric CO and CO_2 from a Global Prediction System during KORUS-AQ Field Campaign, Atmos. Chem. Phys. Discuss., 1–41, doi:10.5194/acp-2018-71, 2018.

Thornton, J. A., Wooldridge, P. J., Cohen, R. C., Martinez, M., Harder, H., Brune, W. H., Williams, E. J. J., Roberts, J. M. M., Fehsenfeld, F. C., Hall, S. R., Shetter, R. E. E., Wert, B. P. and Fried, A.: Ozone production rates as a function of NO_x abundances and HO_x production rates in the Nashville urban plume, J. Geophys. Res., 107(D12), 1–17, doi:10.1029/2001JD000932, 2002.

Tohjima, Y., Kubo, M., Minejima, C., Mukai, H., Tanimoto, H., Ganshin, A., Maksyutov, S., Katsumata, K., Machida, T. and Kita, K.: Temporal changes in the emissions of CH4 and CO from China estimated from CH4 / CO2 and CO / CO2 correlations observed at Hateruma Island, Atmos. Chem. Phys., 14(3), 1663–1677, doi:10.5194/acp-14-1663-2014, 2014.

Ulbrich, I. M., Canagaratna, M. R., Zhang, Q., Worsnop, D. R. and Jimenez, J. L.: Interpretation of organic components from Positive Matrix Factorization of aerosol mass spectrometric data, Atmos. Chem. Phys., 9(9), 2891–2918, doi:10.5194/acp-9-2891-2009, 2009.

Vay, S. A., Tyler, S. C., Choi, Y., Blake, D. R., Blake, N. J., Sachse, G. W., Diskin, G. S. and Singh, H. B.: Sources and transport of Δ14C in CO 2 within the Mexico City Basin and vicinity, Atmos. Chem. Phys., 9, 4973–4985, doi:10.159/acp-9-4973-2009, 2009.

Wang, Y., Munger, J. W., Xu, S., McElroy, M. B., Hao, J., Nielsen, C. P. and Ma, H.: CO_2 and its correlation with CO at a rural site near Beijing: implications for combustion efficiency in China, Atmos. Chem. Phys., 10(18), 8881–8897, doi:10.5194/acp-10-8881-2010, 2010.

Williams, L.: What is My Vaporizer Temperature? Vaporizer Temperature Power Curve for Several Systems, [online] Available from: http://cires1.colorado.edu/jimenez-group/UsrMtgs/UsersMtg11/WilliamsAMSUsersMtg_2010_VapT.pdf (Accessed 12 March 2018), 2010.

Woo, J.-H., An, S.-M., Kim, D.-Y., Kim, H.-K., Choi, K.-C. and Kim, Y.-H.: Development of the Asia Emission Inventory in Support of Integrated Modeling of Climate and Air Quality (III), Incheon, Korea., 2013.

Xu, W., Croteau, P., Williams, L., Canagaratna, M., Onasch, T., Cross, E., Zhang, X., Robinson, W., Worsnop, D. and Jayne, J.: Laboratory characterization of an aerosol chemical speciation monitor with $PM_{2.5}$ measurement capability, Aerosol Sci. Technol., 51(1), 69–83, doi:10.1080/02786826.2016.1241859, 2017.

Xu, W., Lambe, A., Silva, P., Hu, W., Onasch, T., Williams, L., Croteau, P., Zhang, X., Renbaum-Wolff, L., Fortner, E., Jimenez, J. L., Jayne, J., Worsnop, D. and Canagaratna, M.: Laboratory evaluation of species-dependent relative ionization efficiencies in the Aerodyne Aerosol Mass Spectrometer, Aerosol Sci. Technol., 1–16, doi:10.1080/02786826.2018.1439570, 2018.

Yuan, B., Hu, W. W., Shao, M., Wang, M., Chen, W. T., Lu, S. H., Zeng, L. M. and Hu, M.: VOC emissions, evolutions and contributions to SOA formation at a receptor site in eastern China, Atmos. Chem. Phys., 13(17), 8815–8832, doi:10.5194/acp-13-8815-2013, 2013.

Zhang, Q., Stanier, C. O., Canagaratna, M. R., Jayne, J. T., Worsnop, D. R., Pandis, S. N. and Jimenez, J. L.: Insights into the chemistry of new particle formation and growth events in Pittsburgh based on aerosol mass spectrometry, Environ. Sci. Technol., 38(18), 4797–4809, doi:Doi 10.1021/Es035417u, 2004.

Zhang, Q., Alfarra, M. R., Worsnop, D. R., James, D., Coe, H., Canagaratna, M. R. and Jimenez, J. L.: Deconvolution and Quantification of Hydrocarbon-like and Oxygenated Organic Aerosols Based on Aerosol Mass Spectrometry Deconvolution and Quantification of Hydrocarbon-like and

Oxygenated Organic Aerosols Based on Aerosol Mass Spectrometry, Environ. Sci. Technol., 39(13), 4938–4952, doi:10.1021/es048568l, 2005.

Zhao, Y., Hennigan, C. J., May, A. A., Tkacik, D. S., de Gouw, J. A., Gilman, J. B., Kuster, W. C., Borbon, A. and Robinson, A. L.: Intermediate-volatility organic compounds: a large source of secondary organic aerosol, Environ. Sci. Technol., 48(23), 13743–50, doi:10.1021/es5035188, 2014.